A universal model for the permeability of sintered materials

Fabian B Wadsworth, Jérémie Vasseur, Michael J Heap, Lucille Carbillet, Thierry Reuschlé, Patrick Baud, Donald Dingwell

Acta Materialia 250 (2023) 118859

Contents lists available at ScienceDirect

Acta Materialia

journal homepage: www.elsevier.com/locate/actamat

A universal model for the permeability of sintered materials

Fabian B. Wadsworth [a,*], Jérémie Vasseur [b,*], Michael J. Heap [c,d,*], Lucille Carbillet [c], Donald B. Dingwell [b], Thierry Reuschlé [c], Patrick Baud [c]

[a] Earth Science, Durham University Science Labs, Durham DL1 3LE, United Kingdom
[b] Earth & Environmental Science, Ludwig-Maximilians-Universität, Theresienstr. 41, Munich 80333, Germany
[c] Université de Strasbourg, CNRS Institut Terre et Environnement de Strasbourg, UMR 7063, 5 rue René Descartes, Strasbourg F-67084, France
[d] Institut Universitaire de France (IUF), 1 rue Descartes, Paris 75231, France

ARTICLE INFO

Keywords:
Fluid flow
Ergun
Forchheimer
Darcy
Porous media
Sintering

ABSTRACT

Sintered materials are used as permeable filters and flow controllers, for which a validated and general model of porosity and permeability is required. Here, we prepare samples built from mono- and polydisperse glass bead populations sintered for known times at high temperature, and then measure the sample porosity and permeability. We supplement our new dataset with published permeability data for sintered systems including high-temperature *in situ* determinations of permeability during sintering. We test a range of mathematical models for the change in permeability with porosity as sintering progresses from a value for the initial granular particle packing geometry, down to the percolation threshold at low porosity. We find good agreement between our datasets and a preferred theoretical approach – a percolation theory model – with no explicit requirement for empirical adjustment. However, we propose semi-empirical steps that generalize this theory to a universal description across all porosities. Finally, we quantify the inertial component of fluid transport at high flow rates through these materials. Our model framework is made available via a user-friendly downloadable spreadsheet which takes particle size distribution as an input and provides permeability as an output.

1. Introduction

Permeable flow between sintering particles is important in a range of natural, industrial, and theoretical contexts. These applications include the development and design of porous ceramics or glass filters [1–7], precision control of aerostatic porous bearings [8], the sintering of hot volcanic ash deposits during eruptions [9–12], the engineering of lunar regolith [13,14] and the formation of chondrules and planetesimals [15], among many others. Fundamentally, the permeability of particulate systems, including sintering systems, is important for a general understanding of heterogeneous porous media and their percolative, hydraulic properties [1,16–20] as well as for validating cross-property relationships [17].

Regardless of the geometry of the porous medium, the relationship between the pore fluid pressure gradient ∇p and the steady-state filtration fluid velocity $\langle u \rangle$ for a fluid flowing through a porous medium is the Forchheimer equation which has the form $\nabla p = -\alpha_1 \langle u \rangle - \alpha_2 \langle u \rangle^2$, where α_1 and α_2 are both properties of the solid-fluid system [21,22]. Defining $\alpha_1 = \mu_f / k$ and $\alpha_2 = \rho_f / k_I$, where μ_f is the dynamic viscosity of the pore fluid, k is the permeability, ρ_f is the fluid density, and k_I is the inertial permeability, the Forchheimer equation is

$$\nabla p = -\frac{\mu_f}{k} \langle u \rangle - \frac{\rho_f}{k_I} \langle u \rangle^2. \quad (1)$$

Assuming that fluid properties μ_f and ρ_f are well constrained, Eq. (1) suggests that the two material properties of a sintering system that are required are k (SI units: m^2) and k_I (SI units: m); both of which can be expected to be functions of the porosity ϕ [7,23]. There are well-known examples of calibrated proposed semi-empirical forms of Eq. (1) for which k and k_I are replaced with constitutive models; the best known of which is the Ergun equation [24]. However, the prescription of specific forms for k and k_I require validation for each microstructure type in turn and this remains unknown for sintered materials. A key complexity is that in sintering systems, while particles start in a packed particulate state, they evolve as the particle contact areas grow into necks, encroaching on the pore space between the particles. The result is that the porosity decreases non-linearly with time, the specific surface area changes, the microstructure evolves, and the end-state is that of a

* Corresponding authors.
E-mail addresses: fabian.b.wadsworth@durham.ac.uk (F.B. Wadsworth), j.vasseur@lmu.de (J. Vasseur), heap@unistra.fr (M.J. Heap).

https://doi.org/10.1016/j.actamat.2023.118859
Received 14 June 2022; Received in revised form 10 March 2023; Accepted 13 March 2023
Available online 16 March 2023

low-porosity dense and consolidated material [1,5,25–28]. Therefore, any model for the permeability of sintering systems should capture this microstructure change from particulate to non-particulate. Additionally, as sintering approaches completion, the pore space transitions from inter-connected to isolated [1], implying that the permeability drops to zero at a finite porosity termed the percolation threshold ϕ_c.

Here, using experimentally produced sintered materials at a wide range of ϕ and using particles of different starting sizes, we constrain k, k_I, and ϕ_c, testing each against theoretical models or constraints. In doing so, we aim to bring together existing published data for permeable flow through sintered materials, and to formulate a dimensionless framework in which systems of different initial conditions (e.g. different particle sizes or types) can be cross-compared easily and universally.

2. Model development

We first describe existing models for the permeability, inertial permeability, pore space geometry, and specific surface area, which can then be tested by experiment. The aim here is to present models that can be cast in terms of easy-to-measure initial properties of sintering systems only, so that they are of the widest utility. The form of these models guides our experimental campaign designed to test them.

2.1. Models for permeability of sintered materials

Permeability is a function of the porosity ϕ of a medium, but the specific relationship $k(\phi)$ depends on the geometry of the pore network. In sintering systems, this geometry begins as that of particles packed together sharing contact points, and as sintering progresses, evolves to that of pores in a matrix [5,28]. This microstructure evolution has been referred to as a topological inversion because it involves the shift from particles in a gas phase to a gas phase (bubbles) in a matrix such that the curvature of the gas-matrix interface ends the inverse from the start-state [1,29]. This inversion is the basis of sintering models that split the process into an initial stage in which particles form necks with one another [26] and a second stage in which pores between particles shrink [27]. While this two-stage model is not strictly necessary to describe the kinetics of sintering [5], especially for sintering systems that start from highly polydisperse particle size distributions [25], it is conceptually useful for categorizing permeability models into two classes: (1) those that are derived for flow between particles; and (2) those that are derived for flow through so-called 'tight' convolute or complex porous networks. It would seem reasonable to assume that the porosity-dependence of permeability is initially described by a model derived for packed particles, and that as sintering progresses, the permeability moves to a model for other porous network geometries [1].

2.2. Permeability in particulate systems

The most widely used model for the permeability of packs of particles is the so-called Kozeny-Carman relationship [30–32]

$$k = \frac{\phi^3}{Cs^2} \tag{2}$$

where C is a constant and s is the specific surface area at a given porosity; $C = 5$ is found to be valid for packs of spheres mono- or polydisperse in size [31]. Eq. (2) is versatile via the introduction of an adjustable parameter C (and often other empirical adjustments such as 'tortuosity') and has been used widely to describe permeable flow through packs at porosities around $0.2 \lesssim \phi \lesssim 0.6$ [30,31].

Eq. (2) is derived on theoretical grounds, but is semi-empirical, requiring adjustment for particles of a given shape or size distribution via C. By contrast, for the case of spheres arranged in a cubic array, there are purely theoretical approaches that require no adjustment [33,34] and for which validation exists [1,32,35]. For example, Sangani & Acrivos [33] obtained an asymptotic series expansion of the form

$$k = k_s \left[\sum_{i=0}^{30} c_i \left(\frac{1-\phi}{\phi_m} \right)^{i/3} \right]^{-1} \tag{3}$$

where k_s is the Stokes permeability for the dilute limit $\phi \to 1$, c_i are the expansion coefficients (reported elsewhere for $0 < i \leq 30$ for different cubic arrangements [32,33]) and ϕ_m is the porosity at the maximum packing of spheres (for cubic packing arrangements, ϕ_m is well defined depending on the cubic packing type). The scaling factor of the Stokes permeability used in Eq. (3) is $k_s = 2(1-\phi)/s^2$. As with Eqs. (2), (3) can be made specific by introducing a relationship between s at a given porosity, and the particle size or size distribution. We note that Eq. (3) is specifically derived for 'hard', non-overlapping spheres – for which $s(\phi)$ can be derived (discussed later) – but that s in k_s provides a possible method for semi-empirical extension beyond the realm of explicit validity. Taken together, Eqs. (2) & (3) represent two laws for the 'particulate' systems considered here.

2.3. Permeability in non-particulate systems with a percolation threshold

For non-particulate systems that may be suited to the intermediate-to-late stages of sintering, the permeability does not depend strictly on a particle radius, and instead will depend on a pore radius or pore-throat radius describing the width of the connected channels in the tight pore network. In this regime, so-called percolation theories typically yield $k(\phi)$ relationships of with the form $k \propto s^{-2}(\phi - \phi_c)^b$ where b is a percolation exponent and the porosity is scaled down by the percolation threshold [10,11,16,31]. A specific formulation was proposed by Martys et al. [16] and is

$$k = k_r(\phi - \phi_c)^b \tag{4}$$

where $k_r = 2[1-(\phi-\phi_c)]/s^2$ is the scaling factor. k_r and k_s are strikingly similar, with only a difference of ϕ_c. Therefore $\phi - \phi_c$ can be thought of as the 'effective porosity' that is principally involved in the percolative flow, and that when $\phi_c = 0$, $k_r = k_s$.

A geometrical analogy has been drawn between the microstructural evolution observed in sintering systems, and that found for systems of freely overlapping spheres randomly generated in 3D domains [32] such that in both cases, ϕ_c is finite and of similar value [32,36,37] at $\phi_c \approx 0.03$, and the exponent b has been empirically constrained [10,16,32] to be $4 \leq b \leq 4.4$. Additionally, the general evolution of connectivity and permeability is phenomenologically similar in both sintering systems and systems of overlapping spheres; for overlapping sphere models of heterogeneous porous media, b has been theoretically derived [38,39] at $b = 4.4$.

Importantly, for real systems of sintering particles, ϕ_c is not necessarily 0.03. Using *in situ* and time-resolved x-ray data, Wadsworth et al. [1] observed directly that $\phi_c = 0.025$ for sintering glass bead samples and was within uncertainty of the final porosity that was observed post-experiment (i.e. all porosity was isolated at the end of the experiment). By contrast, Wadsworth et al. [40] found that ϕ_c appeared to depend on polydispersivity of the particle size distribution, with the most polydisperse distributions reaching the lowest values of ϕ_c (and lower than $\phi_c = 0.03$). In natural systems of sintered materials, ϕ_c can take a wider range of values, up to $\phi_c = 0.09$ in some cases [11,41,42]. In ceramic sintering systems of crystalline particles, $0.041 \leq \phi_c \leq 0.079$ and the final percolation porosity that is isolated is controlled by the geometry of how the pores close off relative to the crystalline structures of each grain [43,44]. While these ranges in ϕ_c are important for sintering dynamics and the ultimate final properties of a fully-sintered solid, when it comes to the evolution of hydraulic properties, these differences in the limiting ϕ_c are relatively small, and have a minor effect on the overall predictive power of percolation models [10,31,45]. For this reason, in the absence of a specific ϕ_c for a given situation,

Wadsworth et al. [10] have advocated for $\phi_c \approx 0.03$ as a value that is both within most ranges observed and consistent with the sphere-model origins of the percolation models for which ϕ_c is required. However, here, we note that if ϕ_c is known or measurable for a given system, then a system-specific value should be used when implementing the percolation model (Eq. (4)). When applying this model herein, we will test the sensitivity to ϕ_c.

2.4. Models for inertial permeability

We aim to test models for k_I by supplementing our datasets with published data in order to perform a meta-analysis on compiled datasets. On dimensional grounds Zhou et al. [46]. noted that $k_I \propto k^{1/2}$ and therefore proposed an heuristic model in which

$$k_I = \gamma k^{\tau/2}. \tag{5}$$

where γ and τ are constants. Using a wide range of data from many microstructure types and across 12 orders of magnitude of k, they concluded that a reasonable match was found for $\gamma \approx 10^{10}$ m$^{1-\tau}$ and $\tau = 3$ with broad bounds on γ from a lower bound of $\gamma = 10^7$ m$^{1-\tau}$ and an upper bound of $\gamma = 10^{13}$ m$^{1-\tau}$. In less general studies that are specific to a given microstructure type [23], Eq. (5) has been used with a fit of $\gamma = 4.75 \times 10^{14}$ m$^{1-\tau}$ and $\tau = 3.74$.

Ergun [24] used the Kozeny-Carman model for permeability (Eq. (2)) along with a formulation for inertial permeability that is similar to the Kozeny-Carman form $k_I = 2R\phi^3/[B(1-\phi)]$ and $B = 1.75$ that, taken together and injected into Eq. (1) give the so-called Ergun equation. We note that previous work on the permeability of sintered materials has cast the Ergun and Forchheimer equations as two different models [7] where in fact the Ergun equation is a specific calibration of the more general Forchheimer equation, as shown here. By rearranging Eq. (2) and using s for monodisperse non-overlapping spheres, we can inject the Kozeny-Carman formulation for k into the Ergun k_I and find $k_I = 18Ck(1-\phi)/(BR) = 6(Ck)^{1/2}\phi^{3/2}/B$. In turn, this confirms that the Ergun equation finds the scaling given by Eq. (5) with $\tau = 1$.

Innocentini [47] surveyed a wide range of data for ceramics for which k_I and k have been constrained and found an empirical fit $k_I = \exp(m_1 k^{m_2})$ with $m_1 = -1.71588$ and $m_2 = -0.08093$. We note that over the range of permeability tested by Zhou et al. [46] (the same range that is typical for sintered materials [1,47]), this empirical exponential law approaches $k_I \propto k^{1/2}$at the upper end of the range of k tested.

2.5. Models for pore sizes and specific surface area s

Section 2.2 & 2.3 highlight that the specific surface area between the two phases – gas and matrix – s is a relevant inverse lengthscale for constraining hydraulic properties of media. In the case of packed particles, this parameter s depends on the particle radius distribution $F(R)$. If the particle radius distribution is monodisperse, then there is a single relevant radius R, and for polydisperse distributions, the polydispersivity can be captured by a dimensionless group S

$$S = \frac{\langle R\rangle\langle R^2\rangle}{\langle R^3\rangle} \tag{6}$$

where $\langle R^n\rangle$ is the nth moment of the particle radius distribution (i.e. $\langle R\rangle$ is the mean, $\langle R^2\rangle$ is the variance, and $\langle R^3\rangle$ is the skewness) and is found from the particle size probability distribution $F(R)$

$$\langle R^n\rangle = \int_0^\infty R^n F(R)\mathrm{d}R. \tag{7}$$

Eq. (6) can be thought of as the ratio specific surface area of a polydisperse system of overlapping spheres, to that of a monodisperse system at the same mean radius $\langle R\rangle$. Note that $S = 1$ is the monodisperse end-member and $S \to 0$ is highly polydisperse. Using Eq. (6), the specific surface area of polydisperse packs of 'hard' or non-overlapping spheres at a given ϕ is

$$s = 3(1-\phi)\frac{\langle R^2\rangle}{\langle R^3\rangle} \tag{8}$$

and for the monodisperse limit at $S = 1$, $s = 3(1-\phi)/\langle R\rangle$. We note that by injecting the monodisperse s into Eq. (2), we recover the more familiar form of the Kozeny-Carman equation $k(\phi) = \phi^3 R^2/(9C(1-\phi)^2)$.

Eq. (8) can be used to predict the specific surface area of packed particles, but does not give the specific surface area *during* sintering. As discussed in Section 2.1, sintering systems evolve during the sintering process from being packs of polydisperse particles toward an internal geometry analogous to overlapping sphere packs. In the case of overlapping sphere packs, Torquato [17] gives $s(R)$ as

$$s = -3\phi\ln(\phi)\frac{\langle R^2\rangle}{\langle R^3\rangle}. \tag{9}$$

During sintering, as porosity decreases toward the percolation threshold, the microstructural inversion means that the pore network is less well described by models for particulate systems, such as those given in Eqs (6)–(9), and better described by pore size distributions and related models. Therefore, in what follows, for completeness, we present summaries of existing models for computing the size of pores between particles.

Torquato [17] and Torquato & Avellaneda [48] provide a rigorous expression for a mean pore radius $\langle a\rangle$ occurring between polydisperse particles in arbitrary packing. Their scheme can be cast for a packing of completely impenetrable 'hard' spheres. This is given in the form of a cumulative probability density $F(\zeta)$ of the pore size distribution for which $\zeta = 1/x = a/R$, where a is the pore radius, defined formally here:

$$F(\zeta) = \frac{e_V(\zeta)}{\phi}, \tag{10}$$

where $e_V(\zeta)$ is a pore nearest-neighbour exclusion probability function. For polydisperse systems, the pore nearest neighbour exclusion probability function is the polydisperse $e_V(\zeta)$ and is [20]

$$e_V(\zeta) = \phi\exp\left(-2S(1-\phi)\left[\frac{z_0}{8}(1+\zeta)^3 + \frac{z_1}{4}(1+\zeta)^2 + \frac{z_2}{2}(1+\zeta)\right]\right), \tag{11}$$

where the coefficients z_n are given by specific solutions, here with a dependence on S and $\langle R^n\rangle$

$$\begin{aligned} z_0 &= \frac{4\phi\langle R\rangle^2[\phi + 3S(1-\phi)] + 8\langle R^2\rangle[S(1-\phi)]^2}{\phi^3\langle R^2\rangle}, \\ z_1 &= \frac{6\phi\langle R\rangle^2 + 9S\langle R^2\rangle(1-\phi)}{\phi^2\langle R^2\rangle}, \\ z_2 &= \frac{3}{\phi}. \end{aligned} \tag{12}$$

To arrive at the polydisperse solution for $\langle a\rangle$ as a function of $\langle R\rangle$, the nth moment of the probability density function of ζ, termed $\langle\zeta^n\rangle$, is then related to the cumulative probability density function $F(\zeta)$ in Eq. (10) by integrating as follows

$$\langle\zeta^n\rangle = n\int_0^\infty \zeta^{n-1}F(\zeta)\mathrm{d}\zeta, \tag{13}$$

hence the mean (i.e. $n = 1$) value of a is $\langle a\rangle = \langle\zeta\rangle/\langle R\rangle$. Using Eqs. (10)–(13), the pore size distribution between monodisperse or polydisperse distributions of particles can be found. While Eqs. (8) & (9) are for particulate systems, we can use the same approach to give the specific

surface area for the pore-based description of the porous network in the case of non-overlapping or overlapping pores as

$$s = 3\phi\frac{\langle a^2\rangle}{\langle a^3\rangle} \tag{14a}$$

$$s = -3(1-\phi)\ln(1-\phi)\frac{\langle a^2\rangle}{\langle a^3\rangle}. \tag{14b}$$

To summarize, Eq. 14 can be used to predict the specific surface area not just for the initial pack of particles, but throughout sintering as the grains interact, necks form, and the pores between particles shrink. Wadsworth et al. [10] found excellent agreement between permeability data for natural sandstones and clastic volcanic rocks and Eq. (4), using the definition given by Eq. (14b) for s (albeit the monodisperse equivalent $s = -3(1-\phi)\ln(1-\phi)/a$, for which they used the approach encapsulated in Eqs. (10)–(13) to find a from known values of R).

3. Materials and experimental methods

We use the method described in Wadsworth et al. [4] and in Carbillet et al. [49] to create reproducible cylinders of sintered glass beads at different porosity. In all cases, we use Spheriglass® glass beads. These beads are available in various size distributions which are tuneable by sieving and mixing populations [25,49]. They have a well-defined glass transition temperature interval (dependent on the rate of heating or cooling) [50] above which they are beads (or droplets) of highly viscous liquid. For the glass bead populations, we measured the particle diameter distributions using a Beckman-Coulter LS 230 particle size analyzer. These are given together in Fig. 1. We used a range of distributions that span a range of S (Fig. 1).

The cylinders were cored from sintered blocks to a diameter $d = 20$ mm and ground end-parallel to a nominal length $L = 40$ mm. Once prepared, the samples were washed and vacuum-dried at 40 °C for 24 h. The connected porosity of each sample was calculated using the skeletal volume (the volume of the matrix with isolated pores) measured using a helium pycnometer and the bulk sample volume was measured using a cylindrical geometry assumption $V = L\pi(d/2)^2$ and digital calipers.

The permeability of each sample was measured using a steady-state method in one of two permeameters: (1) a benchtop nitrogen gas permeameter (see Farquharson et al. [51] for a schematic); or (2) a water permeameter (see Heap et al. [52] for a schematic). When using the water permeameter, samples were vacuum dried for 12 h, then saturated with de-aired, deionized water in a vacuum chamber prior to measurement. By using two permeameters, we can test for consistency in our results across very different fluid viscosity values. In both cases, we control the pore fluid pressure gradient ∇p, which was held constant, and compute the resulting $\langle u\rangle$ at steady state by measuring the volume flux Q and taking $\langle u\rangle = Q/[\pi(d/2)^2]$. Q is measured using a flow rate meter (for the gas permeability measurements) or an electric balance (for the water permeability measurements) and ∇p is monitored by measuring the upstream pressure p_1 and allowing the downstream pressure p_2 to be atmospheric pressure. The important difference between the two methods – water or nitrogen permeametry – is associated with the pore fluid compressibility. In the case of liquid water, the pressure gradient ∇p at steady state can be assumed to be linear such that $\nabla p = (p_1 - p_2)/L$. However, in the case of nitrogen gas, the compressibility of the gas is important and so $\nabla p = (p_1^2 - p_2^2)/(2Lp_2)$, as shown in Kushnir et al. [53] and Heap et al. [54]. The acquisition of steady state was confirmed visually by stabilization of the measured Q for an average period of between 0.5 and 10 min (depending on the permeability).

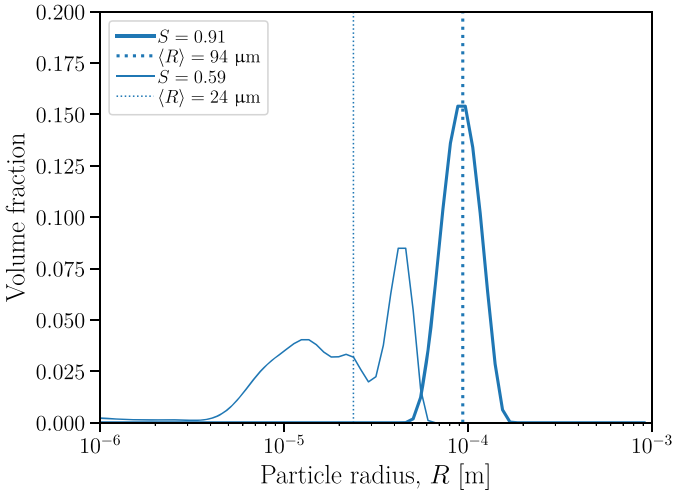

Fig. 1. The particle size distribution of the glass bead populations used in this study. Each distribution is denoted by polydispersivity S. The mean radius $\langle R\rangle$ is given.

4. Results and analysis

Here we present the principal results of our study. First, we present the microstructure evolution and the phenomenology of our quantitative results for samples sintered to different porosities. This forms the basis for our analysis of the efficacy of each constitutive model for $k(\phi)$ and k_I presented in Section 2.

4.1. Microstructure

We take cut, polished cross-sections of sintered samples of glass beads of the size distribution relating to $\langle R\rangle = 23.9$μm (see Fig. 1 for distributions) and for a range of porosities, and photograph them under an optical petrographic microscope. We use Fiji [55] to threshold and binarize the images in order to clearly differentiate the pore space (black) from the glass (white) in Fig. 2. This shows the evolution of pore geometries described qualitatively in Section 2, including the shift from clear particle forms at high porosity (Fig. 2a) to progressively less-particulate forms (Fig. 2b & c) until, at $\phi = \phi_c$ and the termination of sintering, the inversion of the pore geometry to that of vesicles trapped in glass (Fig. 2d). To further characterise the pore fluid geometries, we reproduce 3D computed tomography (resolution 1.7 μm per voxel edge) images of the internal structure of the sintering system in Fig. 2e–h, along with the computed fluid flow pathways at steady-state flow (Fig. 2i–2l; reproduced from Wadsworth et al. [1]; see therein for details). In Fig. 3 we demonstrate that the samples we produce are texturally homogeneous, especially even in the vertical direction parallel to fluid flow in our permeability experiments.

4.2. Fluid flow rates and analysis of k

As predicted by Eq. (1), for a given porosity, the fluid flow rate is proportional to the imposed fluid pressure gradient (Fig. 4), where we perform our analysis using either the compressible (nitrogen) or incompressible (water) description of the pressure gradient (see Section 3). The apparent linearity of $\langle u\rangle$ as a function of ∇p (see Fig. 4a and c) suggests that the second term $(\rho_f\langle u\rangle^2/k_I)$ in Eq. (1) may be negligible for our data, and that therefore our measurements lie in the Darcian, non-inertial regime. This is further evidenced by a secondary analysis in which we can determine an apparent permeability k' for each measurement, where $k' = \mu_f\langle u\rangle/\nabla p$. We find that k' is independent of ∇p, consistent with the Darcian non-inertial regime (see Fig. 4b and d). By fitting Eq. (1) with k and k_I as free fitting parameters, we can find the limiting k values for each sample, which are shown as the values $k' = k$ at $\nabla p \to 0$ (Fig. 4b and d). All raw limiting permeability (i.e. at $\nabla p \to 0$) values are given in the Supplementary Information. This approach is

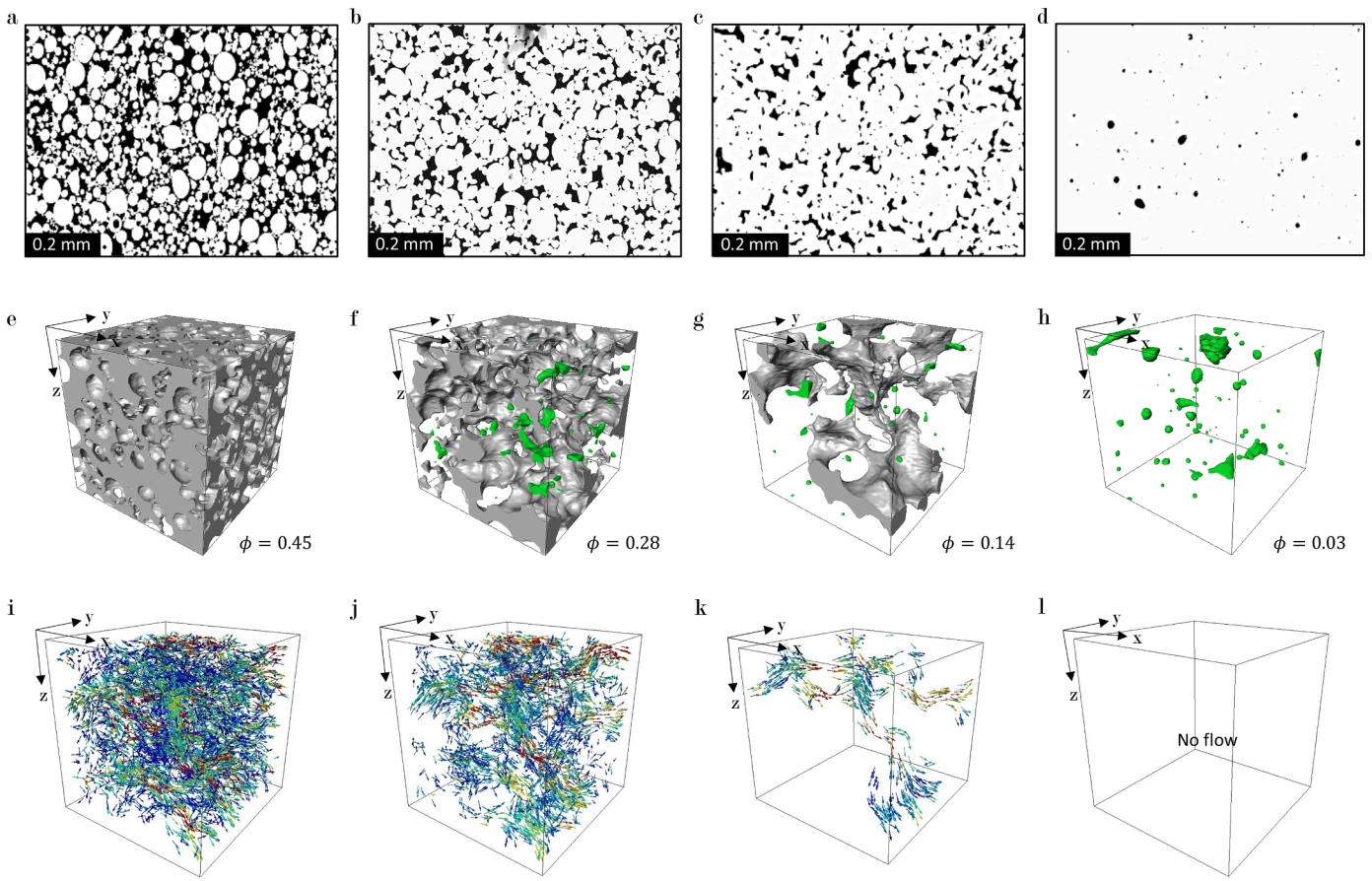

Fig. 2. Cut, polished sections of the internal microstructure of sintered samples of polydisperse glass beads with $\langle R \rangle = 24\mu m$ and $S = 0.59$ (see Fig. 1), at a range of porosity: (a) $\phi = 0.45$; (b) $\phi = 0.28$; (c) $\phi = 0.14$; and (d) $\phi = \phi_c = 0.03$. Black represents pore space and white represents sintered glass. (e–h) Samples at the same porosities as shown in (a–d) but imaged *in situ* during sintering at high temperature using synchrotron-source X-ray computed tomography; grey volumes are connected porosity, green volumes are isolated porosity, and the glass itself is not rendered (transparent). (i–l) Represent the same sample domains as in (e–h) but here the fluid flow vectors at steady state simulated flow through the connected pore volume are shown. Colder colours broadly represent lower fluid speeds relative to warmer colours. Images in panels (a–d) are reproduced from Vasseur et al. [93] and Wadsworth et al. [10] and those in panels (e–l) are reproduced from Wadsworth et al. [1] (with permission in both cases). (For interpretation of the references to colour in this figure legend, the reader is referred to the web version of this article.)

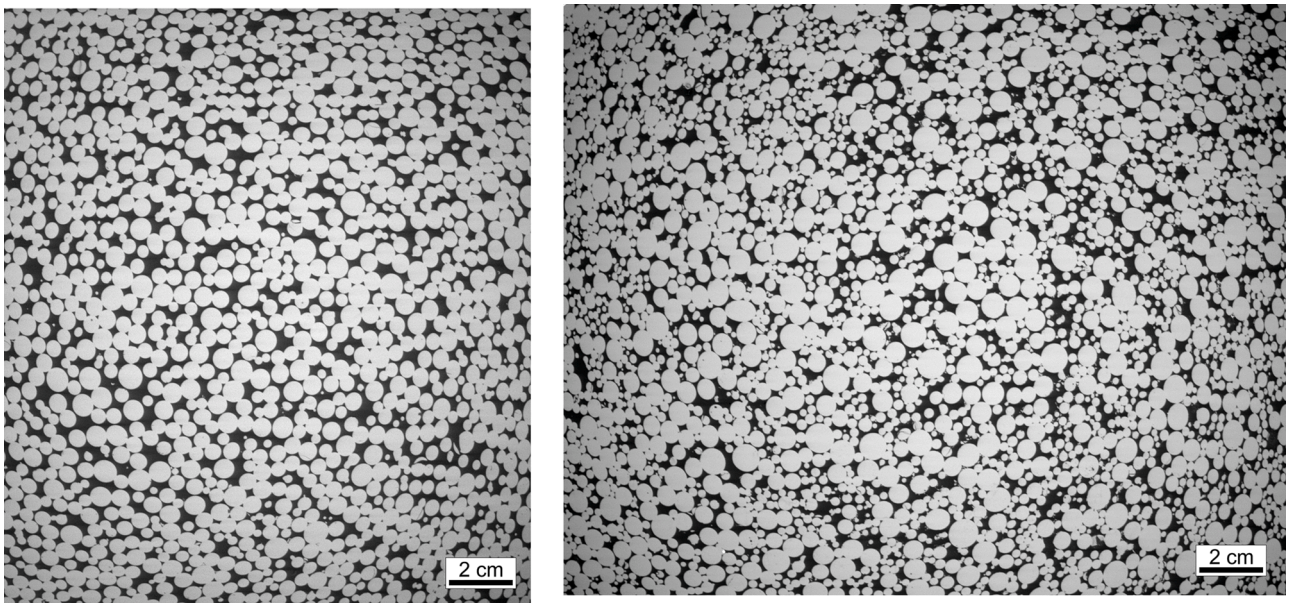

Fig. 3. Low-magnification backscattered SEM images of sintered samples of (left) monodisperse and (right) polydisperse glass bead populations, showing the approximate isotropic nature of the microstructures. For the fluid flow tests, relative flow direction was bottom to top in these images.

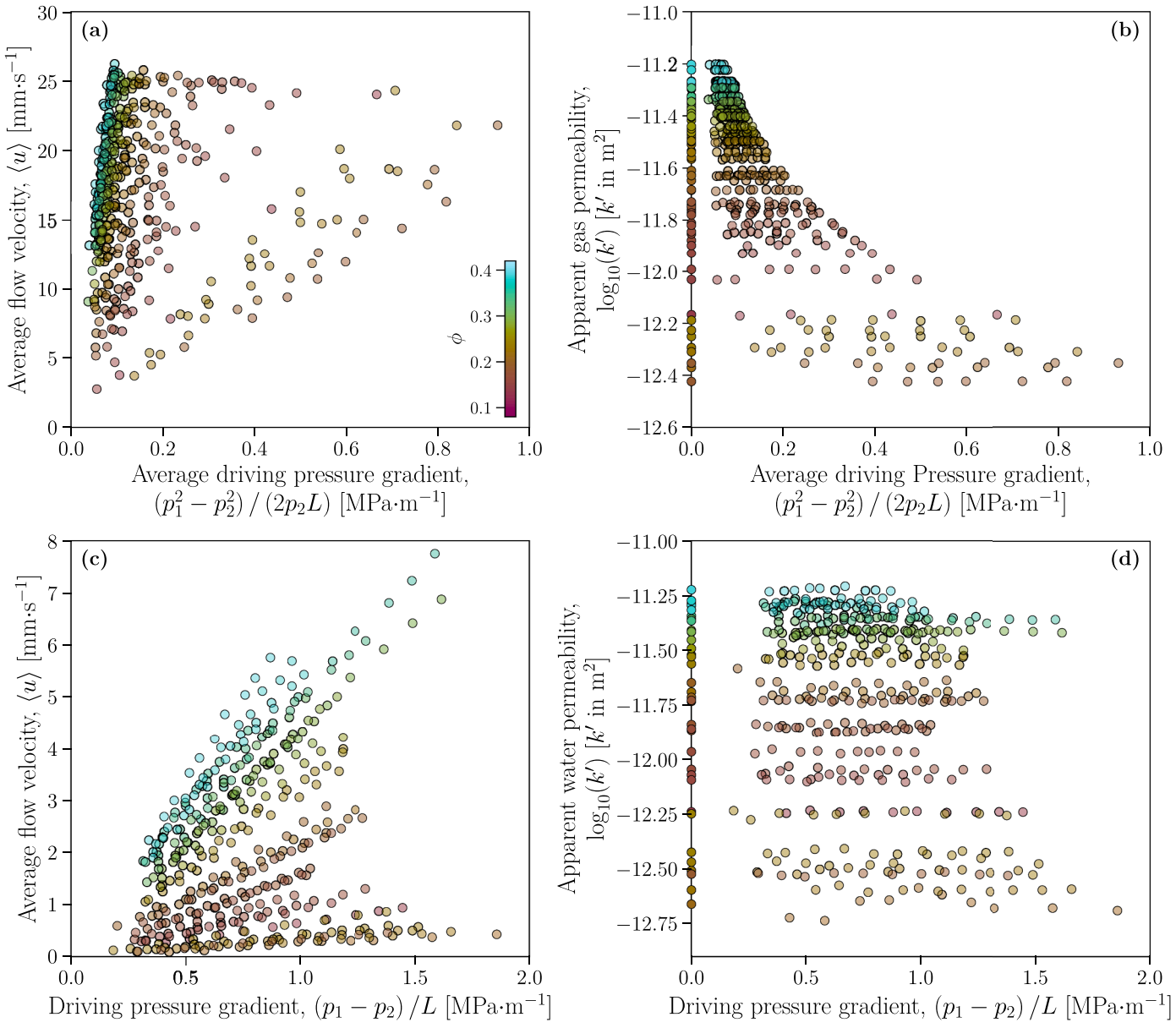

Fig. 4. Examples of the average fluid velocity $\langle u \rangle$ measured at steady state flow for a given imposed pressure difference $p_1 - p_2$ across the sample length L for samples fabricated using both particle size distributions (see Fig. 1) using (a) gas (nitrogen) permeametry $\nabla p = (p_1^2 - p_2^2)/(2p_2L)$ and (c) water permeametry $\nabla p = (p_1 - p_2)/L$. (b-d) The computed apparent permeability $k' = \mu\langle u \rangle / \nabla p$ for each individual steady state measurement as a function of pressure gradient (with the fitted value given on the x-axis origin).

identical to using a so-called 'Forchheimer correction' [54] but without requiring explicit data transformation.

4.3. Testing models for $k(\phi)$

Using the permeability values extracted for each porosity from the raw fluid flow rate data Fig. 4), we can test the models for $k(\phi)$ developed in Section 2. Each model depends on s, and so in principle, each model can be cast for non-overlapping particles (e.g. Eq. (8)) or overlapping particles (Eq. (9)) or for the non-overlapping or overlapping pore equivalents (see Eq. (14a) & (b)). When testing the Kozeny-Carman (Eq. (2)) and the cubic particle packing expansion (Eq. (3)) models, it is clear that these should be solved for the non-overlapping particle case implicit in the model derivation. However, for the percolation theory model (Eq. (4)) there is in principle some conceptual flexibility in how s is computed. However, we posit that the option most consistent with the known internal microstructure changes extant in sintering systems is to assume that the particles are initially impenetrable, in order to use Eqs. (10)–((13) to compute the moments of the pore radius distribution $\langle a \rangle$, $\langle a^2 \rangle$, and $\langle a^3 \rangle$. Because pores are inherently able to overlap with no formal interface between them, the reasonable computation of s is via Eq. (14b) for overlapping pores.

The considerations outlined above provide us with the fully posed three models to test against the $k(\phi)$ data, which are:

$$k = \frac{\phi^3 \langle R^3 \rangle^2}{9C(1-\phi)^2 \langle R^2 \rangle^2}, \tag{15a}$$

$$k = \frac{2\langle R^3\rangle^2}{9(1-\phi)\langle R^2\rangle^2}\left[\sum_{i=0}^{30} c_i\left(\frac{1-\phi}{\phi_m}\right)^{i/3}\right]^{-1}, \tag{15b}$$

$$k = \frac{2[1-(\phi-\phi_c)]\langle a^3\rangle^2}{9[(1-\phi)\ln(1-\phi)]^2\langle a^2\rangle^2}(\phi-\phi_c)^b, \tag{15c}$$

where $\langle R^2\rangle$ and $\langle R^3\rangle$ are measured inputs (i.e. in Eq. (15a)) and are used to compute $\langle a^2\rangle$ and $\langle a^3\rangle$ in Eq. (15c), via Eqs. (10)–(13). While we favour the theoretical $b = 4.4$ value in all applications of Eq. (15c), we treat ϕ_c as a fitting parameter, with the expectation that $\phi_c = 0.03$ is a reasonable value (constrained for overlapping spheres and sintering spherical glass beads [5,32]). We do additionally demonstrate how a co-varying fit of both ϕ_c and b performs.

A key input to our method for converting particle size distributions (cast as volume fractions per bin) to pore size distributions between the particles, is the initial porosity at which the packing of particles occurs prior to sintering ϕ_i. This value is a function of particle polydispersivity S, such that more polydisperse distributions of glass beads pack at a lower initial porosity than their monodisperse counterparts. Using data from Wadsworth et al. [25], we fit an entirely empirical function $\phi_i = x_1(1-S)^{x_2}$ with $x_1 = 0.375 \pm 0.006$ and $x_2 = -0.116 \pm 0.012$ (Fig. 5), showing good agreement. This provides a method by which we can predict ϕ_i for our distributions used herein ($\phi_i = 0.497 \pm 0.017$ for $\langle R\rangle = 94\mu$m and $\phi_i = 0.416 \pm 0.008$ for $\langle R\rangle = 24\mu$m samples). In turn, this allows us to compute the pore size distributions, and therefore the specific surface areas for use with Eq. 15.

We find that in general, for a given particle size or size distribution, the different models derived (e.g. Eq. 15) occupy different portions of the $k(\phi)$ trend for which they provide good predictive power. Importantly, we find no appreciable difference between the water and gas permeability data. This is expected as the compressibility effect was taken into account when computing the gas pressure gradient, and because the water saturation was 100%. The analysis of these data is provided in Fig. 6. The Kozeny-Carman model (Eq. (15a)) provides a reasonable description of our data, although in detail is further from the data at very low porosity where the sintering system is close the percolation threshold, which is consistent with the observation that the Kozeny-Carman model does not include an explicit accounting of the percolation threshold. Similarly, the Kozeny-Carman model diverges from our data at high porosity. The model for the permeability of packs of cubic arrays of spheres (Eq. (15b)) is always above the datasets analysed here and appears not to provide a good description of the data (discussed later).

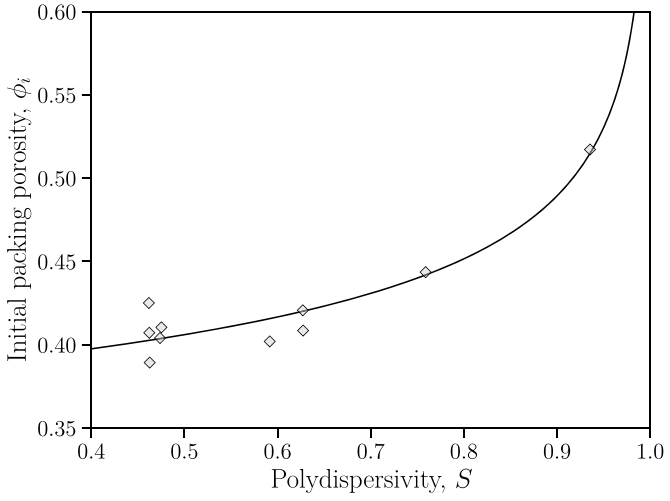

Fig. 5. The relationship between the initial packing porosity ϕ_i and particle polydispersivity S for random packs of glass beads. Data are taken from Wadsworth et al. [25] and fit to a functional form $\phi_i = x_1(1-S)^{x_2}$ with $x_1 = 0.375$ and $x_2 = -0.116$ empirical fit parameters. This empirical fit. Is not valid explicitly at $S = 1$ and is only used here for the distributions investigated at $S < 1$.

The percolation model (Eq. (15c)) with the derived $b = 4.4$ and the widely-used $\phi_c = 0.03$ provides a reasonable description of the $\langle R\rangle = 94\mu$m samples, but overestimates the permeability for the $\langle R\rangle = 24\mu$m samples. If we allow b and ϕ_c to act as free parameters, we are able, for all cases, to obtain excellent agreement with the model. Wadsworth et al. [1] showed that this model is strictly valid at low porosity $\phi < 0.2$ where sintering systems are non-particulate. Therefore, when we restrict the fitting of b and ϕ_c to data in this lower range of ϕ, we find that the best-fit values approach or even converge with the canonical $b = 4.4$ and $\phi_c = 0.03$ (Fig. 6c & d). This provides robust confirmation that the physical underpinning of this model – based in overlapping sphere geometries – is applicable to sintering systems at low porosities, consistent with previous work [1,32] (Fig. 6).

5. Extended validation and model testing

We have tested the validity of each of the component $k(\phi)$ models proposed here Eq. (15) against an extensive dataset that covers a range of polydispersivity S and particle size $\langle R\rangle$ as well as porosity ϕ Table 1). Here, we aim to extend this validation procedure by (1) testing some of the metrics on which our $k(\phi)$ models depend, but which we did not provide new data to test (principally $s(\phi)$ and Eqs. (8) & (9); (2) explore the extent to which there can be universality in our understanding of $k(\phi)$ by developing a single dimensionless description; (3) further test the $k(\phi)$ models but using compiled literature data; and (4) testing $k_I(\phi)$ models for the inertial contributions to permeable flow in sintered porous media.

5.1. Validation of $s(\phi, R)$

In Section 4, we used models for s when computing k. This relies on the assumption that Eqs. (8), (9) and (14) are correct and valid for the systems in question. This is required for most cases because s is not often measured directly. Here, we compile a dataset acquired via *in situ* high temperature sintering of glass beads and obsidian particles, presented previously [1,11] as well as datasets for *ex-situ* sintering [56] and sphere packing simulations [31,32,57] for which data for $s(\phi)$ exist.

The samples used had particle size characteristics $\langle R\rangle$, $\langle R^2\rangle$, and $\langle R^3\rangle$ reported which can be used to compute the moments of the pore size distribution via Eqs. (10)–(13). The internal structures of the sintering packs of beads and obsidian particles were captured using X-ray computed tomography during sintering directly, and s was determined using a marching cubes algorithm [58] on the segmented pore-glass interfaces.

In Fig. 7, we test these sample and simulation geometries against Eqs. (8), (9), and (14). In order to test these universally, regardless of the size of the particles or spheres used, we normalize the specific surface area to find a dimensionless specific surface area $\bar{s}$, so that Eqs. (8), (9) and (14b) become

$$\bar{s} = \frac{s\langle R^3\rangle}{\langle R^2\rangle} = 3(1-\phi), \tag{16a}$$

$$\bar{s} = \frac{s\langle R^3\rangle}{\langle R^2\rangle} = -3\phi\ln(\phi), \tag{16b}$$

$$\bar{s} = \frac{s\langle a^3\rangle}{\langle a^2\rangle} = -3(1-\phi)\ln(1-\phi). \tag{16c}$$

We find that the hard sphere simulations follow Eq. (16a), as expected. Similarly, we find that the overlapping sphere simulations follow either Eq. (16b) or 16c depending on whether ϕ refers to the inter-sphere or the

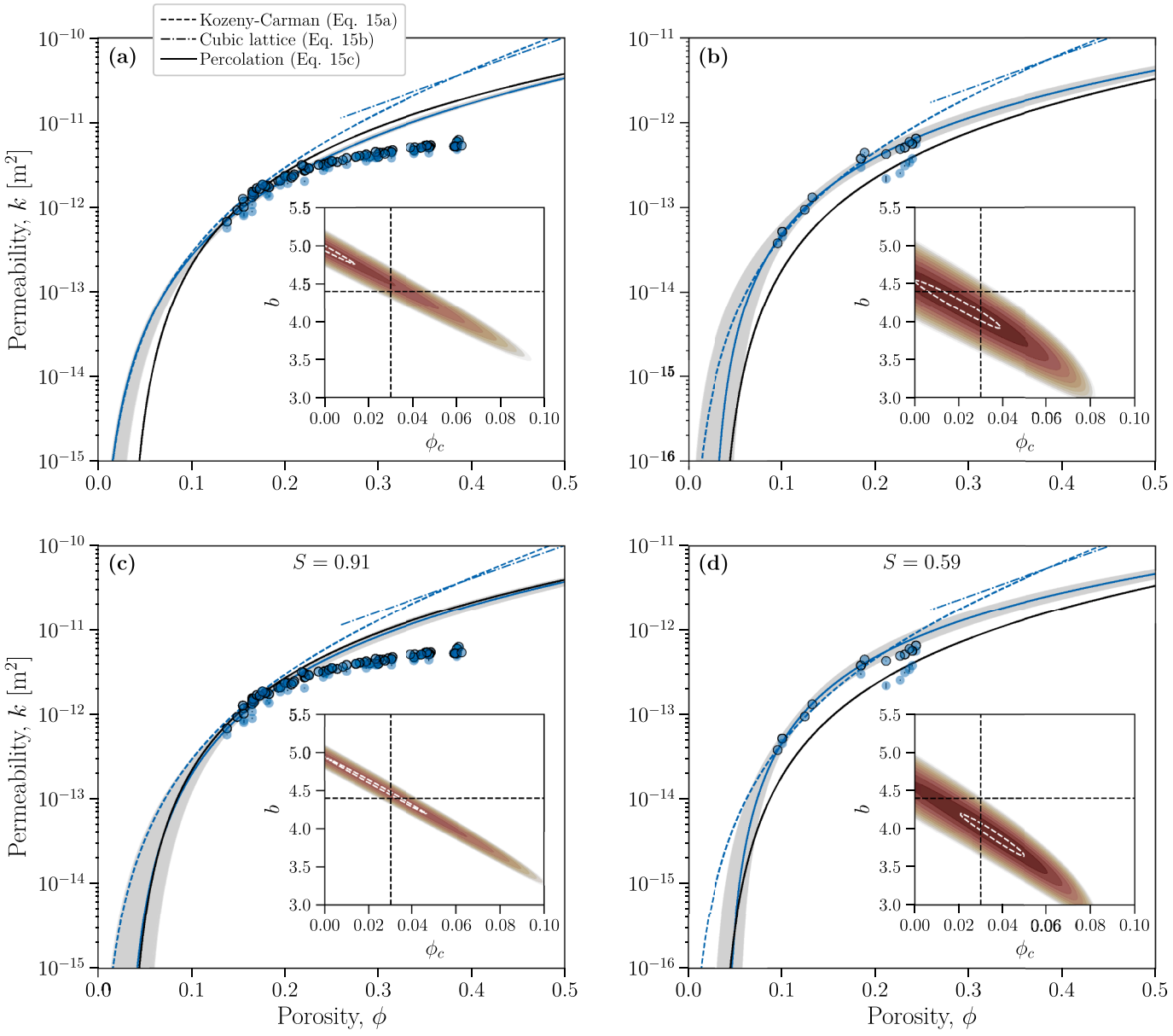

Fig. 6. The experimentally determined gas (solid outlines) and water (no outlines) permeability data as a function of the porosity for (a) the $S = 0.91$ samples and (b) the $S = 0.59$ samples. Shown here are each of the constitutive models that we propose herein. The Kozeny-Carman model (Eq. (15a)) and the cubic lattice model (Eq. (15b)) are shown with no fitting parameters (e.g. with the previously constrained $C = 5$ for the Kozeny-Carman model). We only show the FCC lattice result for the cubic lattice model type, noting that the BCC and SC results are strikingly similar [31,32]. The percolation model (Eq. (15c)) is shown using the 'standard parameters' of $b = 4.4$ and $\phi_c = 0.03$ validated previously for sintering systems [1,10] and for overlapping spheres [32] (solid black curve), as well as the best-fit model for $\phi \leq 0.25$ and for which we allow b and ϕ_c to covary – these are given by the solid coloured curve (best-fit) and the grey band ($\pm 2\sigma$; note that the grey band does not show unphysical solutions for which $\phi_c < 0$). *Inset:* The fit performance for the percolation model inputs, showing the best-fit 2σ ellipse (dashed white curve), contoured for the goodness of fit statistic, and showing the 'standard parameter' inputs for reference (dashed black lines). In the percolation model results presented here, the initial porosity is required to compute s (see text) and is taken to be the value corresponding to the data and model provided in Fig. 5. (c,d) The same as in (a) and (b) but where the percolation model is only fit over the range of data that occur with $0 < \phi \leq 0.2$ corresponding to the expected range of validity of the percolation model (see text).

sphere pore space (the former is reiterated here because this is the inverse definition from that used in one of the studies from which the data are derived [57]). Finally, we find that all sintering systems follow Eq. (16c). This confirms that an inter-particle pore description of sintering systems is more appropriate than a particle-based description, confirming the empirical findings for pore-based sintering kinetic models [5].

5.2. A universal dimensionless description of $k(\phi)$

As well as non-dimensionalizing the specific surface area (Eq. 16), we can also non-dimensionalize the constitutive equations for permeability. To do this, we generalize the Stokes permeability as $k_s = k_r = 2(1-\phi^*)/s^2$, which results in dimensionless versions of each model in turn:

$$\bar{k} = \frac{\phi^3}{2C(1-\phi)} \tag{17a}$$

Table 1

Study identifier	Sintering material	S	$\langle R\rangle$ [m], $\langle R^2\rangle$ [m^2] and $\langle R^3\rangle$* [m^3]	$\langle a\rangle$ [m], $\langle a^2\rangle$ [m^2] and $\langle a^3\rangle$ [m^3] using Eqs. (9)–(12)	ϕ_c used here	Range of k [m^2]
Sintering systems						
Wadsworth et al. [1].	Glass beads	0.90	$\langle R\rangle = 4.09\times10^{-5}$, $\langle R^2\rangle = 1.76\times10^{-9}$, $\langle R^3\rangle = 8.00\times10^{-14}$	$\langle a\rangle = 1.88\times10^{-5}$, $\langle a^2\rangle = 5.26\times10^{-10}$, $\langle a^3\rangle = 1.82\times10^{-14}$	0.03	$1.38\times10^{-14} \le k \le 1.00\times10^{-11}$
Wadsworth et al. [4].	Glass beads	0.91	$\langle R\rangle = 9.41\times10^{-5}$, $\langle R^2\rangle = 9.28\times10^{-9}$, $\langle R^3\rangle = 9.56\times10^{-13}$	$\langle a\rangle = 1.83\times10^{-5}$, $\langle a^2\rangle = 4.97\times10^{-10}$, $\langle a^3\rangle = 1.67\times10^{-14}$	0.03	$3.61\times10^{-13} \le k \le 1.03\times10^{-11}$
Eichheimer et al. [56].	Glass beads	0.99	$\langle R\rangle = 6.02\times10^{-4}$, $\langle R^2\rangle = 3.64\times10^{-7}$, $\langle R^3\rangle = 2.21\times10^{-10}$	$\langle a\rangle = 1.10\times10^{-4}$, $\langle a^2\rangle = 1.79\times10^{-8}$, $\langle a^3\rangle = 3.59\times10^{-12}$	0.03	$5.70\times10^{-15} \le k \le 3.10\times10^{-11}$
Gueven et al. [59].	Glass beads	0.94	$\langle R\rangle = 2.44\times10^{-4}$, $\langle R^2\rangle = 6.16\times10^{-8}$, $\langle R^3\rangle = 1.60\times10^{-11}$	$\langle a\rangle = 6.57\times10^{-5}$, $\langle a^2\rangle = 6.32\times10^{-9}$, $\langle a^3\rangle = 7.44\times10^{-13}$	0.03	$1.16\times10^{-10} \le k \le 2.75\times10^{-10}$
Wong et al. [60].	Glass beads	~1	$4.85\times10^{-5} \le \langle R\rangle \le 1.94\times10^{-4}$	$1.05\times10^{-5} \le \langle a\rangle \le 4.21\times10^{-5}$	0.03	$2.98\times10^{-16} \le k \le 8.57\times10^{-12}$
Glass & Green [63]	Ceramics	n.d.	n/a	$\langle a\rangle = 5.00\times10^{-8}$	0.03	$5.30\times10^{-19} \le k \le 2.50\times10^{-17}$
AmesPore®	Metal beads	n.d.	n/a	$1.17\times10^{-5} \le \langle a\rangle \le 2.18\times10^{-4}$	0.03	$1.16\times10^{-12} \le k \le 7.48\times10^{-10}$
Natural systems						
Ryan et al. [64].	Volcanic rock powder	n.d.	$\langle R\rangle = 1.00\times10^{-5}$	$\langle a\rangle = 1.84\times10^{-6}$	0.03	$1.18\times10^{-15} \le k \le 4.04\times10^{-14}$
Wadsworth et al. [11].	Angular obsidian particles	0.60	$\langle R\rangle = 2.33\times10^{-5}$, $\langle R^2\rangle = 7.66\times10^{-10}$, $\langle R^3\rangle = 2.96\times10^{-14}$	$\langle a\rangle = 8.01\times10^{-6}$, $\langle a^2\rangle = 9.40\times10^{-11}$, $\langle a^3\rangle = 1.35\times10^{-15}$	0.03	$1.17\times10^{-13} \le k \le 7.93\times10^{-12}$
Zhang et al. [65].	Angular calcite particles	n.d.	$\langle R\rangle = 5.00\times10^{-6}$	$\langle a\rangle = 2.64\times10^{-7}$	0.03	$1.17\times10^{-20} \le k \le 9.77\times10^{-17}$
Bernabé et al. [66].	Angular calcite particles	n.d.	n/a*	$\langle a\rangle = 1.50\times10^{-7}$	0.03	$5.25\times10^{-20} \le k \le 5.04\times10^{-17}$
Bourbie & Zinszner[71]	Sandstones	n.d.	$\langle R\rangle = 2.50\times10^{-4}$	$\langle a\rangle = 2.05\times10^{-5}$	0.03	$7.46\times10^{-17} \le k \le 7.70\times10^{-12}$
Okumura & Sasaki[69]	Angular obsidian particles	n.d.	$\langle R\rangle = 1.25\times10^{-4}$	$\langle a\rangle = 1.34\times10^{-5}$	0.03	$1.58\times10^{-15} \le k \le 1.00\times10^{-12}$
Heap et al. [67].	Polymict volcanic particles	n.d.	$\langle R\rangle = 2.50\times10^{-5}$	$\langle a\rangle = 1.80\times10^{-6}$	0.03	$6.14\times10^{-16} \le k \le 1.41\times10^{-13}$
Giger et al. [68].	Quartz particles	n.d.	$\langle R\rangle = 1.00\times10^{-6}$	$\langle a\rangle = 8.70\times10^{-8}$	0.03	$1.40\times10^{-21} \le k \le 4.43\times10^{-17}$

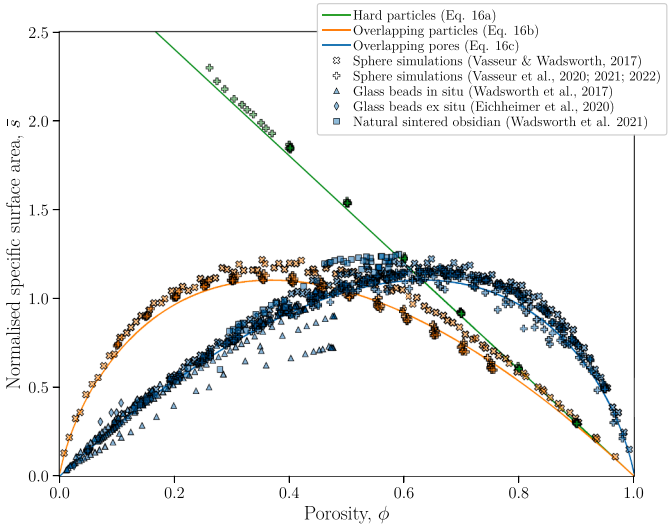

Fig. 7. The normalized specific surface area $\bar{s}$ as a function of porosity ϕ, which is required to use the suite of model solutions proposed here (e.g. Fig. 6). Shown here are direct measurements of $\bar{s}$ made using *in situ* synchrotron-source X-ray tomography data for the evolving internal structure of glass beads [1] and obsidian particles [11] sintering in real time. Additional *ex situ* data are shown for sintered glass bead samples [56], overlapping sphere simulations [32,57], and hard sphere simulations [31]. The models shown here are given by Eq. (16). The normalization for the datasets is given by either $\bar{s} = s\langle R^3\rangle / \langle R^2\rangle$ or $\bar{s} = s\langle a^3\rangle / \langle a^2\rangle$.

$$\bar{k} = \left[\sum_{i=0}^{30} c_i \left(\frac{1-\phi}{\phi_m}\right)^{i/3}\right]^{-1} \tag{17b}$$

$$\bar{k} = (\phi - \phi_c)^b \tag{17c}$$

where the normalization is $\bar{k} = k/k_s$. Note that here our definition of k_s uses ϕ^* in place of ϕ, where $\phi^* = \phi$ for the hard-sphere models Eq. (17a) & (17b), but $\phi^* = \phi - \phi_c$ for the percolation model Eq. (17c), which is an approach used previously for experimental data [1] and sphere simulations [45]. Eq. 17 represents a proposed universal framework for examining the permeability of porous media composed of particles, of which sintering systems are a part. Eq. 17 leaves open some flexible choices available in terms of how the data are normalized to the models, in terms of which $s(\phi)$ model is used; here we use the models most appropriate (via the analysis in Fig. 7).

5.3. Comparison with published sintering data

Here, we can test the efficacy of the models proposed using available published data for sintering systems that, cumulatively, cover a very wide range of particle sizes, distributions, and polydispersivity, as well as variable sintering processes, materials, and dynamic techniques. The core datasets used here include other studies that have utilized sintered glass bead systems [4,32,56,59,60], studies in which the sintering particles were metals [7,61,62], including Amespore® company data, and ceramic particles[63]. Additional to these core datasets, we compile data for the permeability of natural sintered products or experimental reproductions of natural sintering [11,64–69], which includes systems

of sintering hot volcanic ash, volcanic glass, and crystalline particles, sintering calcite particles, or sintering quartz particles in geological faults under pressure. Finally, we compile data for numerical simulations of the permeability of simplified geometries that have been proposed to represent sintering microstructures, which include random heterogeneous systems of overlapping spheres [32] and hard spheres [31], and cubic lattice systems of hard spheres [1,32,35,70]. In all cases, we provide the microstructural information required to apply Eq. 17 to these data in Table 1.

While not a sintering system *per se*, we also compile data for clean quartz-rich sandstones over a wide range of ϕ from Bourbié & Zinszner [71]. This follows Wadsworth et al. [10] and Carbillet et al. [49], who proposed that the diagenetic processes involved in the densification and lithification of clay-free sedimentary rocks is microstructurally similar to sintering processes. This comparison with sandstone data has the additional benefit that the Bourbié & Zinszner[71] data include determinations of k at values of ϕ very close to ϕ_c, representing a good test of the model at the low-porosity limit.

When taken together, and regardless of the models, we find that all data collapse to a universal trend of $k(\phi)$ when k is normalized by k_s (Fig. 8). To achieve this, we use $\phi^* = \phi - \phi_c$ for all data except the hard sphere simulations for which ϕ_c is undefined and taken to be zero (see Table 1 for the ϕ_c values used here). Additionally, informed by Fig. 7, we use Eq. (14b) (or equivalently Eq. (16c)) to find $s(\phi)$ for sintering data, which, by comparing with Eq. (17a), suggests why the cubic packing model did not agree with our experimental data shown in Fig. 6. We conclude that if the explicit derivation of Eq. (3) (or (17b)) is relaxed, and $s(\phi)$ for overlapping pores between hard packed spheres is used in place of formally hard spheres, then sintering systems agree with the cubic packing model at high porosities (Fig. 8). In turn, this is broadly consistent the topological inversion conclusion for sintering systems[1] which predicts that at their high porosity limit, they are more like hard particles.

When comparing this collapse to the universal models in Eq. 17, we can see that there is a continuous transition with decreasing porosity from the hard sphere model for the permeability of cubic packs (Eq. (17b)) to the percolation theory model at low porosity (Eq. (17c)). Importantly, while the modified Kozeny-Carman model (Eq. (17a)) fits the data adequately or well for intermediate porosities, the range of the whole system in which it could be said to be predictive, is limited. We suggest that the wide use of that model is perhaps because the range of porosity in which it does work ($0.2 \lesssim \phi \lesssim 0.6$) coincides with the range of porosity which packed particle systems such as engineering soils and sands occupy. Our normalized result also suggests that the microstructure of very loose, high porosity packs of particles is indistinguishable from cubic lattice packs and that the role played by random heterogeneity at high porosity is minor in terms of the resistance to flow.

The analysis presented here suggests that there may be universality in the evolution of sintering systems, which, when normalized in the manner proposed, will always evolve from a particulate description to a porous, percolation-theory description (Fig. 8). We therefore find no requirement for pore microstructure descriptors such as tortuosity [56], changepoints at which empirical power laws move from one exponent to another [51], or effective porosities reduced from measured porosities [56]. Instead, we find that the specific surface area is an adequate inverse length scale for a wide range of pore geometries in terms of the controlling length scale for percolative flow, and that the percolation threshold is required to scale down the effective pore volume available for flow at any moment in the sintering process.

5.4. Inertial effects

In order to test the effects of inertia on the flow rates through sintered samples, we re-fit the raw $\langle u \rangle (\nabla p)$ data from Zhong et al. [7]. for sintered metal particles, for which their flow rates included values sufficiently high for non-Darcian flow to become important. This allows us to find k_I via minimization to Eq. (1). Following previous work [23,46], we look for the trend of k_I as a function of k, in order to test Eq. (5) (Fig. 9). We supplement these data with data from published work on explicitly sintered systems [7,61,62,72] as well as general porous ceramics including gel-cast foams and castables [47,73–82], and a range of other porous media [83]. We do not find a global log-linear relationship, as predicted by Eq. (5). Instead, we find that these data appear to map out an empirical form $k_\mathrm{I} = \exp(m_1 k^{m_2})$ with $m_1 = -1.71588$ and $m_2 = -0.08093$ after Innocentini [47]. We do find that the Zhou et al. [46] model provides a good description at high or low permeability with $\tau \approx 1$ and $\tau \approx 5$, respectively (Fig. 9).

We use Eq. (1) to analyse the data from our experimental work. In doing so, we use the ∇p relevant for the incompressible or compressible gas for water and nitrogen analyses respectively (see Section 3). For each of the component fits for Eq. (1), we treat both k and k_I as free fit parameters and use a least squares regression analysis technique to find the best-fit values of these parameters. We find that the majority of our data show a broadly linear relationship between ∇p and $\langle u \rangle$, implying that the second term on the right-hand side of Eq. (1) (i.e. $\alpha_2 \langle u \rangle^2$) is negligible. Inertial effects dominate the permeable flow of fluid if the Reynolds number Re of the fluid flow in the porous medium is high ($\mathrm{Re} \gg 1$). Conversely, if $\mathrm{Re} \ll 1$, then $\alpha_2 \to 0$, in which case Eq. (1) reduces to Darcy's law $\nabla p = -\mu_f \langle u \rangle / k$. The Reynolds number Re is locally variable and depends on the local fluid velocity and the local lengthscale, and therefore it is not trivial to define for a given fluid flow scenario. However, using only the macroscopic property relations, we can define a variant of Re, which we term a Forchheimer number Fo [21,23] and which characterizes the bulk average fluid flow through the medium

$$\mathrm{Re} \approx \mathrm{Fo} = \frac{\rho_f}{\mu_f} \frac{k}{k_\mathrm{I}} \langle u \rangle \tag{18}$$

such that Darcy's law is the valid limiting solution at $\mathrm{Fo} \ll 1$. Eq. (18) implies that a useful lengthscale dictating the balance of inertial and viscous forces in the fluid is $L = k/k_\mathrm{I}$ and that the useful velocity is the bulk filtration velocity $\langle u \rangle$, which both have the advantage that they can be determined from experimental or numerical results directly. In order to compare data for $\langle u \rangle$ and ∇p across a wide variety of material properties, porous media microstructures, and Fo conditions, a so-called dimensionless friction factor f can be defined as

$$f = \frac{\nabla p k_\mathrm{I}}{\rho_f \langle u \rangle^2} \tag{19}$$

which can be used to normalize experimental data. Data normalized using Eq. (19) can be compared with a universal model relationship $f(\mathrm{Fo})$ has the form [7,83,84]

$$f = \frac{1}{\mathrm{Fo}} + 1. \tag{20}$$

which essentially represents a non-dimensional form of Eq. (1). In Fig. 10 we test Eq. (20) against data normalized using Eqs. (18) & (19). In doing so, we use the best-fit k values for each sample with a given ϕ. Then for the Zhong et al. [7] data for which k_I could be determined directly, we use the best-fit k_I values, and for our samples we use the empirical law proposed via the analysis presented in Fig. 9 to find k_I from k. We find excellent agreement between these datasets and Eq. (20), which in turn represents an apparently universal and dimensionless description of fluid flow through sintered samples and allows samples of any porosity to be compared.

5.5. Frontiers and outlook

We have principally validated a sequence of constitutive models (e.g. Eqs. (5), (15), & (17)) that allow Eq. (1) to be solved for any sintered

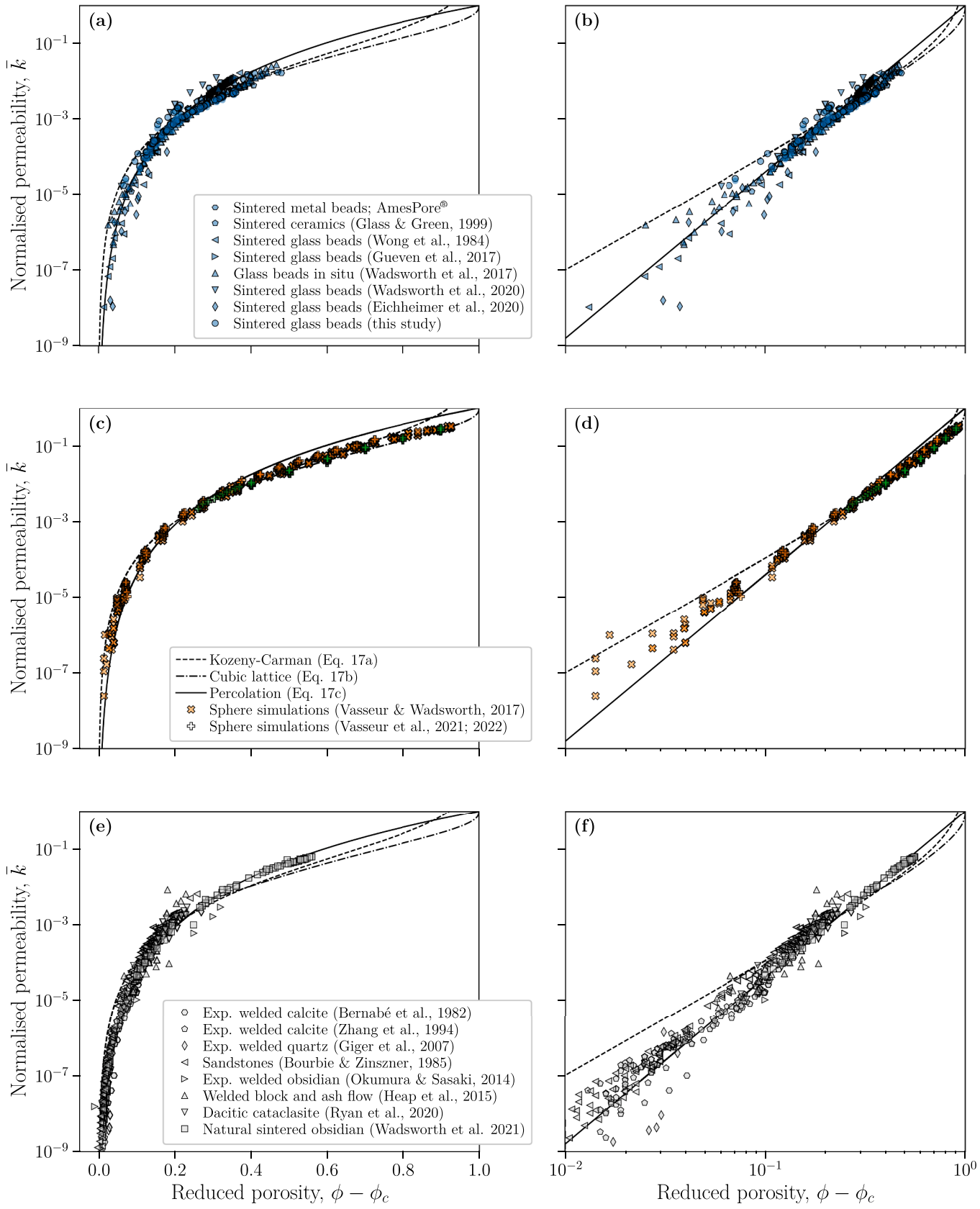

Fig. 8. Testing the efficacy of our universal description of permeability via $\bar{k} = k/k_s$ and our reduction of porosity via $\phi - \phi_c$. The panels are divided into (a,b) sintering systems, (c,d) sphere simulations, and (e,f) natural or more complex systems. In all cases, the right-hand column is simply a log-log version of the same plots in the left-hand column, for clarity.

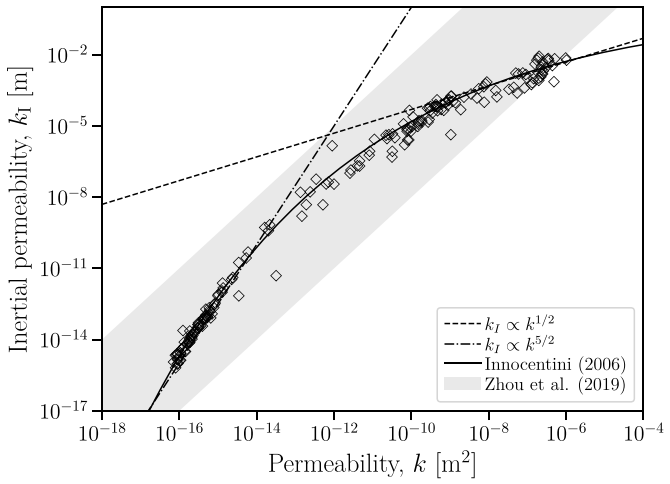

Fig. 9. The inertial permeability k_I (non-Darcian) as a function of the permeability k (Darcian). Data compiled here include explicitly sintered systems [7,61,62,72] as well as general porous ceramics including gel-cast foams and castables[47], [73–82], and a range of other porous media [83]. We additionally show (1) the best-fit empirical model $k_I = \exp(m_1 k^{m_2})$ with $m_1 = -1.71588$ and $m_2 = -0.08093$ after Innocentini [47], (2) a general range of power-law scaling laws for geological materials of the form $k_I = Ak^{3/2}$ (given by the grey band that is bounded by $10^7 < A < 10^{13}$) [46], and (3) two limiting scaling approaches $k_I \propto k^{5/2}$ and $k_I \propto k^{1/2}$, which appear to be consistent with the data, for which the latter $k_I \propto k^{1/2}$ is dimensionally consistent.

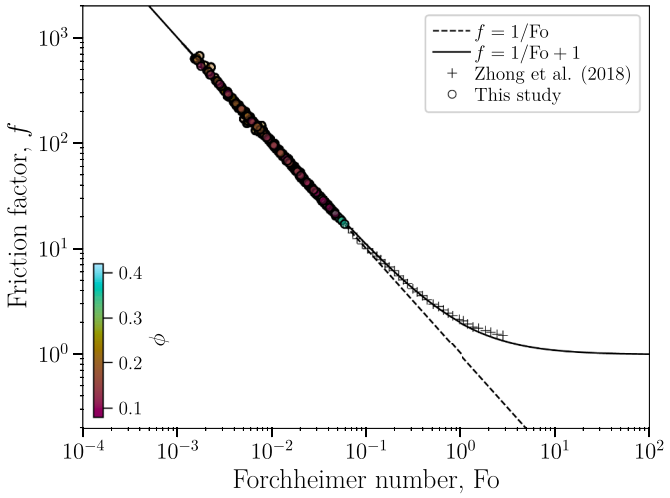

Fig. 10. The dimensionless description of the fluid flow behaviour through sintered materials described by the friction factor f and the Forchheimer number Fo. For the data presented in this study, we use the empirical law $k_I = \exp(m_1 k^{m_2})$ from Fig. 9 to find k_I from k for each sample porosity. Shown here are the Darcian regime $f = 1/\mathrm{Fo}$ and the full Darcian-to-non-Darcian law $f = 1/\mathrm{Fo} + 1$.

sample at a known ϕ. We have used glass and metal sphere sintered samples as a core validation sample type, but extended our validation step to samples sintered from particles of non-isometric shapes and roughness, including natural samples sintered from volcanic ash or diagenetically formed from sand particles by processes in the Earth's crust. We propose that this represents a stern test of these models, and therefore the utility and predictive power of the result is general. There are several considerations that would represent important extensions of this model, which are explored briefly here.

Importantly, we have not explicitly validated these models for sintered ceramics. This will be a key area into which these models could be extended and validated in future. Based on the excellent performance of these models against such a wide range of complex systems and materials, we can be reasonably confident that this general framework will be effective for ceramic sintering. However, some key areas may require development. For example, the value of the percolation threshold – important for the percolation model given here – can be substantially higher than the 0.03 value proposed here [43,44]. Similarly, and for similar reasons, the specific surface area evolution for ceramic sintering could deviate from the sphere-systems approaches given here. If this deviation occurs, it seems likely that it would be most pronounced at low porosities, where the pore closure events occur around faceted and strongly non-spherical crystalline grains, rather than the smoother pore-edges that occur at the end of a viscous sintering process. While these features of ceramic sintering models would need further testing, we suggest that once ϕ_c and $s(\phi)$ are validated, Eq. 17 can be used for these systems.

In this study we use the Forchheimer equation (Eq. (1)) to relate the pressure gradient to the resultant flow rate through porous media. In Eq. (1) we deal with the viscous term proposed by Darcy [85] and the inertial term proposed by Forchheimer [22]. However, we note that there are additional terms that could be considered, related to the phase shift between transient pressure gradients and the acceleration of the fluid in the inertial regime [86,87]. These are not relevant for the steady-state permeability determinations in systems of small relative length, and we note that the additional terms do not involve additional constants to be determined. Therefore, for inertial flow in larger systems these terms could be added and a more complete description of the fluid flow could be used as

$$\nabla p = -\frac{\mu_f}{k}\langle u\rangle - \frac{\rho_f}{k_I}\langle u\rangle^2 - \frac{\rho}{\phi}\left(\frac{\partial\langle u\rangle}{\partial z} + \frac{\langle u\rangle}{\phi}\frac{\partial\langle u\rangle}{\partial z}\right) \tag{21}$$

which represents the Navier-Stokes momentum equation for porous media. Here, z is the position locally in the porous medium in the direction of the pressure gradient. If sintered materials are used as filters at high and unsteady flow rates, then Eq. (21) may be necessary to solve for the fluid flow rates as a function of the driving pressure gradient, and the constraints for k and k_I provided herein are sufficient to pose the problem. This would require explicit validation. A similar consequence of considering larger sintered systems is that the sintering fabrication process is likely to be subject to buoyancy-driven gravity waves, which manifest as porosity variations in the material that is produced (e.g. see predictions by Wadsworth et al. [9] for sintering systems that are larger than the so-called 'compaction length' and related explicit numerical models [88]). Therefore, there is scope to explore the effect of these real processes on the length-averaged permeability in large sintered systems, as well as implications for permeability anisotropy development.

The majority of the materials considered herein are sintered in the viscous state – e.g. glass bead particles or angular glass fragments – such that the microstructural evolution is one of viscous neck formation, particle wall smoothing, and pore closure (e.g. Fig. 2). While we do include some data in our compilation collected by solid-state sintering, driven by diffusion of mass toward particle-particle contacts [64], it is possible that microstructural evolution differs from glass systems, in terms of $s(\phi)$. Future work could explore this regime more thoroughly. Similarly, some sintering systems of wide interest involve mixtures of glass and crystalline (rigid and non-sintering) particles [89,90], with the existing observation that sintering to very low porosity is halted when there are substantial fractions of non-sintering 'obstacle particles' in the mixture. The implications of such mixtures for permeability remains unknown, but it seems likely that if the porosity is halted from the usual end-state of $\phi \rightarrow \phi_c$, then the permeability may also be held to a non-zero equilibrium. This would represent 'propped' systems that do not close effectively, and could be stable. More work is required to investigate such mixed systems.

Our model validation includes natural sandstone data, however the

data selected is for sandstones that do not host pore-filling clays or pore coatings. Such clays and coatings can be common in sedimentary basins and could be expected to modify $s(\phi)$ from the idealized descriptions given herein [91]. Similarly, in 'tight' sandstones or other sedimentary rocks for which the pore sizes are especially small, the so-called Klinkenberg gas-slip effect can become important. Future work could further explore the similarities between sintering granular-to-non-granular systems and sedimentary rock-forming systems that encompasses these complexities. The Klinkenberg effect can be theoretically incorporated into Eq. (1) via a modification of the Darcy term as [41,54,92]

$$\nabla p = -\frac{\mu_f}{k}\langle u\rangle K - \frac{\rho_f}{k_1}\langle u\rangle^2 \tag{22}$$

where $K = 1 + 2\omega/(p_2 + p_1)$ is a Klinkenberg correction term with the Klinkenberg 'slip factor' ω. The parameter K becomes important at low porosities or small pore sizes, such that sintering systems could be expected to approach the Klinkenberg regime in which gas slippage effects are important as sintering completes and $\phi \rightarrow \phi_c$.

Finally, and perhaps most relevant to both industrial filtration models and natural environments of reactive fluid flow, the application of these permeability models to systems in which there are diffusion-precipitation-leaching reactions that could occur during permeable flow, involving the modification of both the pore-solid interface quality, and the pore sizes and throat sizes, is a key frontier. This introduces the potential for both time-dependence, and spatial variability during flow, as well as being a key process that dictates the utility lifetime of a sintered filter.

6. Concluding remarks

We have sought to validate constitutive models that, when applied together, provide a framework for predicting fluid flow rates through sintered materials. We conclude that sintered materials are geometrically closely analogous to systems of random and heterogeneous overlapping spheres, such that models for the percolative flow between such systems provides an excellent description. Importantly, we have taken a step-by-step approach to our analysis, in order to arrive at a universal description in dimensionless form, which permits us to compile a large test-database for robust validation across a wide range of all input parameters. In the Supplementary Information to this contribution, we provide a Microsoft Excel© spreadsheet (in .xlsx form) of our preferred model (preferred on the basis of fit performance), which can be used to predict fluid flow rates for a range of given simple-to-determine input parameters ($F(R)$ and ϕ_c).

Funding statement

Funding was provided by ERC ADV 2018 Grant 834255 (EAVESDROP), and the Natural and Environmental Sciences Research Council (NERC) via grant NE/T007796/1.

Supplementary material

See supplementary material for the complete raw datasets used herein for the flow rate as a function of driving pressure gradient data, and for the downloadable Excel™ implementation of the models proposed here for sintering systems.

Declaration of Competing Interest

The authors declare no competing interests.

Acknowledgments

We thank Jenny Schauroth, Yan Lavallée, Anthony Lamur, and Jackie Kendrick for stimulating discussion, and Betty Scheu and Mathieu Colombier for laboratory assistance in an early iteration of sample fabrication. Simon Lejart is thanked for laboratory assistance at Strasbourg. We acknowledge the Paul Scherer Institute for awarding beamtime grants under proposals 20141231 and 20150413 which resulted in some of the datasets reproduced and analysed in this contribution [1]. M. Heap acknowledges support from the Institut Universitaire de France (IUF).

Supplementary materials

Supplementary material associated with this article can be found, in the online version, at doi:10.1016/j.actamat.2023.118859.

References

[1] F.B. Wadsworth, J. Vasseur, E.W. Llewellin, et al., Topological inversions in coalescing granular media control fluid-flow regimes, Phys. Rev. E 96 (3) (2017), 033113, https://doi.org/10.1103/PhysRevE.96.033113.
[2] N. Taoka, K. Ohno, T. Komori, S. Hirota, Y. Ogura, T. Tanaka, K. Itoh, Porous Ceramic Sintered Body and Method of Producing the same, and Diesel Particulate Filter, undefined, Google Patents, 2004. n.d.
[3] J. Adler, Ceramic diesel particulate filters, Int. J. Appl. Ceram. 2 (6) (2005) 429–439, https://doi.org/10.1111/j.1744-7402.2005.02044.x.
[4] F.B. Wadsworth, C.E.J. Vossen, D. Schmid, et al., Determination of permeability using a classic darcy water column, Am. J. Phys. 88 (1) (2020) 20–24, https://doi.org/10.1119/10.0000296.
[5] F.B. Wadsworth, J. Vasseur, E.W. Llewellin, et al., Sintering of viscous droplets under surface tension, Proc. R. Soc. A Math. Phys. Eng. Sci. 472 (2188) (2016), 20150780, https://doi.org/10.1098/rspa.2015.0780.
[6] B.L. Krasnyi, V.P. Tarasovskii, A.Y. Val'dberg, T.O. Kaznacheeva, Porous permeable ceramics for filter elements cleaning hot gases from dust, Glass Ceram. 62 (5–6) (2005) 134–138, https://doi.org/10.1007/s10717-005-0056-7 (English Transl Steklo i Keramika).
[7] W. Zhong, X. Ji, C. Li, J. Fang, F Liu, Determination of permeability and inertial coefficients of sintered metal porous media using an isothermal chamber, Appl. Sci 8 (9) (2018) 1670, https://doi.org/10.3390/app8091670.
[8] R. Nicoletti, Z.C. Silveira, B.M. Purquerio, Modified reynolds equation for aerostatic porous radial bearings with quadratic forchheimer pressure-flow assumption, J. Tribol. 130 (3) (2008), https://doi.org/10.1115/1.2919776.
[9] F.B. Wadsworth, J. Vasseur, J. Schauroth, et al., A general model for welding of ash particles in volcanic systems validated using *in situ* X-ray tomography, Earth Planet Sci. Lett. 525 (2019), 115726, https://doi.org/10.1016/j.epsl.2019.115726.
[10] F.B. Wadsworth, J. Vasseur, B. Scheu, J.E. Kendrick, Y. Lavallée, D.B. Dingwell, Universal scaling of fluid permeability during volcanic welding and sediment diagenesis, Geology 44 (3) (2016) 219–222, https://doi.org/10.1130/G37559.1.
[11] F.B. Wadsworth, J. Vasseur, E.W. Llewellin, et al., A model for permeability evolution during volcanic welding, J. Volcanol. Geotherm. Res. 409 (2021), 107118, https://doi.org/10.1016/j.jvolgeores.2020.107118.
[12] F.B. Wadsworth, E.W. Llewellin, J. Vasseur, J.E. Gardner, H. Tuffen, Explosive-effusive volcanic eruption transitions caused by sintering, Sci. Adv. 6 (39) (2020) eaba7940, https://doi.org/10.1126/sciadv.aba7940.
[13] H. Toutanji, C.M. Goff, E. Ethridge, E. Stokes, Gas permeability and flow characterization of simulated lunar regolith, Adv. Space Res. 49 (8) (2012) 1271–1276, https://doi.org/10.1016/j.asr.2012.02.002.
[14] A. Meurisse, J. Beltzung, M Kolbe, Influence of mineral composition on sintering lunar regolith, J. Aerosp. (2017).
[15] S. Sirono, Planetesimal formation induced by sintering, Astrophys. J. Lett. 733 (2) (2011) 41.
[16] N.S. Martys, S. Torquato, D.P. Bentz, Universal scaling of fluid permeability for sphere packings, Phys. Rev. E 50 (1) (1994) 403.
[17] S. Torquato, Random Heterogeneous materials: Microstructure and Macroscopic Properties, Springer Science & Business Media, 2013.
[18] P.C.G. Carman, Fluid flow through granular beds, Trans. Inst. Chem. Eng. 75 (Suppl) (1937) 150–166, https://doi.org/10.1016/s0263-8762(97)80003-2.
[19] J. Kozeny, Uber kapillare leitung der wasser in boden, Sitzungsberichte Kais. Akad. Wiss. Wien 136 (1927) 271–306.
[20] S. Torquato, B. Lu, Rigorous bounds on the fluid permeability: effect of polydispersivity in grain size, Phys. Fluids A Fluid Dyn. 2 (4) (1990) 487–490.
[21] Z. Zeng, R. Grigg, A criterion for non-darcy flow in porous media, Transp. Porous Media 63 (1) (2006) 57–69, https://doi.org/10.1111/j.1439-0523.2006.01169.x.
[22] P Forchheimer, Wasserbewegung durch Boden, Z. Ver. Dtsch. Ing. 45 (1) (1901) 1782–1788, https://doi.org/10.1016/S0022-0728(70)80153-X.
[23] A.C. Rust, K.V. Cashman, Permeability of vesicular silicic magma: inertial and hysteresis effects, Earth Planet Sci. Lett. 228 (1–2) (2004) 93–107, https://doi.org/10.1016/j.epsl.2004.09.025.
[24] S. Ergun, Fluid flow through packed columns, Chem. Eng. Prog. 48 (1952) 89–94, citeulike-article-id:7797897.
[25] F.B. Wadsworth, J. Vasseur, E.W. Llewellin, D.B. Dingwell, Sintering of polydisperse viscous droplets, Phys. Rev. E 95 (3) (2017), 033114, https://doi.org/10.1103/PhysRevE.95.033114.

[26] J. Frenkel, Viscous flow of crystalline bodies under the action of surface tension, J. Phys. 9 (5) (1945) 385–391.
[27] J.K. Mackenzie, R. Shuttleworth, A phenomenological theory of sintering, Proc. Phys. Soc. Sect. B 62 (12) (1949) 833.
[28] M. Prado, E. Dutra Zanotto, R Müller, Model for sintering polydispersed glass particles, J. Non Cryst. Solids 279 (2) (2001) 169–178.
[29] G. Okuma, D. Kadowaki, T. Hondo, S. Tanaka, F. Wakai, Interface topology for distinguishing stages of sintering, Sci. Rep. 7 (1) (2017) 11106, https://doi.org/10.1038/s41598-017-11667-2.
[30] M. Röding, Z. Ma, S. Torquato, Predicting permeability via statistical learning on higher-order microstructural information, Sci. Rep. 10 (1) (2020) 1–17, https://doi.org/10.1038/s41598-020-72085-5.
[31] J. Vasseur, F.B. Wadsworth, J.P. Coumans, D.B. Dingwell, Permeability of packs of polydisperse hard spheres, Phys. Rev. E 103 (6) (2021) 62613, https://doi.org/10.1103/PhysRevE.103.062613.
[32] J. Vasseur, F.B. Wadsworth, Sphere models for pore geometry and fluid permeability in heterogeneous magmas, Bull. Volcanol. 79 (11) (2017) 77, https://doi.org/10.1007/s00445-017-1165-1.
[33] A.S. Sangani, A. Acrivos, Slow flow through a periodic array of spheres, Int. J. Multiph. Flow 8 (4) (1982) 343–360, https://doi.org/10.1016/0301-9322(82)90047-7.
[34] H. Hasimoto, On the Periodic Fundamental Solutions of the Stokes equations and Their Application to Viscous Flow Past a Cubic Array of Spheres, undefined, Researchgate.net, 1959. n.d.
[35] E.W. Llewellin, LBflow: an extensible lattice Boltzmann framework for the simulation of geophysical flows. part i: theory and implementation, Comput. Geosci. 36 (2) (2010) 115–122, https://doi.org/10.1016/j.cageo.2009.08.004.
[36] M.D. Rintoul, Precise determination of the void percolation threshold for two distributions of overlapping spheres, Phys. Rev. E 62 (1) (2000) 68.
[37] J. Kertesz, Percolation of holes between overlapping spheres: monte Carlo calculation of the critical volume fraction, J. Phys. Lett. 42 (17) (1981) 393–395.
[38] S. Feng, B.I.B. Halperin, P.N.P. Sen, Transport properties of continuum systems near the percolation threshold, Phys. Rev. B 35 (1) (1987) 197–214, https://doi.org/10.1103/PhysRevB.35.197.
[39] B.I. Halperin, S. Feng, P.N. Sen, Differences between lattice and continuum percolation transport exponents, Phys. Rev. Lett 54 (22) (1985) 2391–2394, https://doi.org/10.1103/PhysRevLett.54.2391.
[40] F.B. Wadsworth, J. Vasseur, E.W. Llewellin, D.B. Dingwell, Sintering of polydisperse viscous droplets, Phys. Rev. E 95 (3) (2017), https://doi.org/10.1103/PhysRevE.95.033114.
[41] M.J. Heap, H. Tuffen, F.B. Wadsworth, T. Reuschlé, J.M. Castro, C.I. Schipper, The permeability evolution of tuffisites and implications for outgassing through dense rhyolitic magma, J. Geophys. Res. Solid Earth 124 (8) (2019) 8281–8299, https://doi.org/10.1029/2018jb017035.
[42] M. Colombier, F.B. Wadsworth, B. Scheu, et al., *In situ* observation of the percolation threshold in multiphase magma analogues, Bull. Volcanol. 82 (4) (2020) 32, https://doi.org/10.1007/s00445-020-1370-1.
[43] T. Spusta, J. Svoboda, K. Maca, Study of pore closure during pressure-less sintering of advanced oxide ceramics, Acta Mater. 115 (2016) 347–353, https://doi.org/10.1016/j.actamat.2016.05.049.
[44] J. Svoboda, H. Riedel, H. Zipse, Equilibrium pore surfaces, sintering stresses and constitutive equations for the intermediate and late stages of sintering—I. computation of equilibrium surfaces, Acta Metall. Mater. 42 (2) (1994) 435–443, https://doi.org/10.1016/0956-7151(94)90498-7.
[45] J. Vasseur, F.B. Wadsworth, E. Bretagne, D.B. Dingwell, Universal scaling for the permeability of random packs of overlapping and nonoverlapping particles, Phys. Rev. E 105 (4) (2022), L043301, https://doi.org/10.1103/PhysRevE.105.L043301.
[46] J.Q.Q. Zhou, Y.F.F. Chen, L. Wang, M.B. Cardenas, Universal relationship between viscous and inertial permeability of geologic porous media, Geophys. Res. Lett. 46 (3) (2019) 1441–1448, https://doi.org/10.1029/2018GL081413.
[47] M. Scheffler, P. Colombo, Cellular ceramics : structure, Manufacturing, Properties and Applications, 2005, p. 645.
[48] S. Torquato, M. Avellaneda, Diffusion and reaction in heterogeneous media: pore size distribution, relaxation times, and mean survival time, J. Chem. Phys. 95 (9) (1991) 6477–6489.
[49] L. Carbillet, M.J. Heap, P. Baud, F.B. Wadsworth, T. Reuschlé, Mechanical compaction of crustal analogs made of sintered glass beads: the influence of porosity and grain size, J. Geophys. Res. Solid Earth 126 (4) (2021), e2020JB021321, https://doi.org/10.1029/2020JB021321.
[50] F.B. Wadsworth, J. Vasseur, F.W. Aulock, et al., Nonisothermal viscous sintering of volcanic ash, J. Geophys. Res. Solid Earth 119 (12) (2014) 8792–8804.
[51] J.I. Farquharson, M.J. Heap, Y. Lavallée, N.R. Varley, P. Baud, Evidence for the development of permeability anisotropy in lava domes and volcanic conduits, J. Volcanol. Geotherm. Res. 323 (2016) 163–185, https://doi.org/10.1016/j.jvolgeores.2016.05.007.
[52] M.J. Heap, Y. Lavallée, L. Petrakova, et al., Microstructural controls on the physical and mechanical properties of edifice-forming andesites at Volcán de Colima, Mexico, J. Geophys. Res. Solid Earth 119 (4) (2014) 2925–2963, https://doi.org/10.1002/2013JB010521.
[53] A.R.L. Kushnir, C. Martel, R. Champallier, F.B. Wadsworth, Permeability evolution in variably glassy basaltic andesites measured under magmatic conditions, Geophys. Res. Lett. 44 (20) (2017) 10, https://doi.org/10.1002/2017GL074042, 210-262,271.
[54] M.J. Heap, A.R.L. Kushnir, H.A. Gilg, F.B. Wadsworth, T. Reuschlé, P. Baud, Microstructural and petrophysical properties of the permo-triassic sandstones (buntsandstein) from the soultz-sous-forêts geothermal site (France), Geotherm. Energy 5 (1) (2017) 26, https://doi.org/10.1186/s40517-017-0085-9.
[55] J. Schindelin, I. Arganda-Carreras, E. Frise, et al., Fiji: an open-source platform for biological-image analysis, Nat. Methods 9 (7) (2012) 676–682, https://doi.org/10.1038/nmeth.2019.
[56] P. Eichheimer, M. Thielmann, W. Fujita, et al., Combined numerical and experimental study of microstructure and permeability in porous granular media, Solid Earth 11 (3) (2020) 1079–1095, https://doi.org/10.5194/se-11-1079-2020.
[57] J. Vasseur, F.B. Wadsworth, D.B. Dingwell, Permeability of polydisperse magma foam, Geology 48 (6) (2020) 536–540, https://doi.org/10.1130/G47094.1.
[58] T. Lewiner, H. Lopes, A.W. Vieira, G. Tavares, Efficient implementation of marching cubes' cases with topological guarantees, J. Graph Tools 8 (2) (2003) 1–15, https://doi.org/10.1080/10867651.2003.10487582.
[59] I. Gueven, S. Frijters, J. Harting, S. Luding, H. Steeb, Hydraulic properties of porous sintered glass bead systems, Granul. Matter 19 (2) (2017) 28, https://doi.org/10.1007/s10035-017-0705-x.
[60] P. Wong, J. Koplik, J.P. Tomanic, Conductivity and permeability of rocks, Phys. Rev. B 30 (11) (1984) 6606–6614, https://doi.org/10.1103/PhysRevB.30.6606.
[61] Y. Liao, X. Li, W. Zhong, G. Tao, H. Liu, T. Kagawa, Experimental study of pressure drop-flow rate characteristics of heated tight porous materials, J. Fluids Eng. 138 (7) (2016), https://doi.org/10.1115/1.4032751.
[62] Y. Liao, X. Li, W. Zhong, G. Tao, Study of pressure drop-flow rate and flow resistance characteristics of heated porous materials under local thermal non-equilibrium conditions, Int. J. Heat Mass Transf. 102 (2016) 528–543, https://doi.org/10.1016/j.ijheatmasstransfer.2016.05.101.
[63] S.J. Glass, D.J. Green, Permeability and infiltration of partially sintered ceramics, J. Am. Ceram. Soc. 82 (10) (1999) 2745–2752, https://doi.org/10.1111/j.1151-2916.1999.tb02151.x.
[64] A.G. Ryan, J.K. Russell, M.J. Heap, M.E. Zimmerman, F.B. Wadsworth, Timescales of porosity and permeability loss by solid-state sintering, Earth Planet Sci. Lett. 549 (2020), 116533, https://doi.org/10.1016/j.epsl.2020.116533.
[65] S. Zhang, M.S. Paterson, S.F. Cox, Porosity and permeability evolution during hot isostatic pressing of calcite aggregates, J. Geophys. Res. Solid Earth 99 (B8) (1994) 15741–15760, https://doi.org/10.1029/94JB00646.
[66] Y. Bernabe, W.F. Brace, B. Evans, Permeability, porosity and pore geometry of hot-pressed calcite, Mech. Mater. 1 (3) (1982) 173–183, https://doi.org/10.1016/0167-6636(82)90010-2.
[67] M.J. Heap, J.I. Farquharson, F.B. Wadsworth, S. Kolzenburg, J.K. Russell, Timescales for permeability reduction and strength recovery in densifying magma, Earth Planet Sci. Lett. 429 (2015) 223–233, https://doi.org/10.1016/j.epsl.2015.07.053.
[68] S.B. Giger, E. Tenthorey, S.F. Cox, J.D Fitz Gerald, Permeability evolution in quartz fault gouges under hydrothermal conditions, J. Geophys. Res. Solid Earth 112 (B7) (2007), https://doi.org/10.1029/2006JB004828.
[69] S. Okumura, O. Sasaki, Permeability reduction of fractured rhyolite in volcanic conduits and its control on eruption cyclicity, Geology 42 (10) (2014) 843–846.
[70] E.W. Llewellin, LBflow: an extensible lattice Boltzmann framework for the simulation of geophysical flows. part II: usage and validation, Comput. Geosci. 36 (2) (2010) 123–132, https://doi.org/10.1016/j.cageo.2009.08.003.
[71] T. Bourbie, B. Zinszner, Hydraulic and acoustic properties as a function of porosity in Fontainebleau sandstone, J. Geophys. Res. Solid Earth 90 (B13) (1985) 11524–11532.
[72] M.V. Gerotto, A.R. Studart, M.D.M. Innocentini, Kaolin, metakaolin and microsilica as fillers for high-alumina refractory castables, Am. Ceram. Soc. Bull. 81 (9) (2002) 40–47.
[73] M.D.M. Innocentini, P. Sepulveda, V.R. Salvini, V.C. Pandolfelli, J.R. Coury, Permeability and structure of cellular ceramics: a comparison between two preparation techniques, J. Am. Ceram. Soc. 81 (12) (1998) 3349–3352, https://doi.org/10.1111/j.1151-2916.1998.tb02782.x.
[74] E.A. Moreira, M.D.M. Innocentini, J.R. Coury, Permeability of ceramic foams to compressible and incompressible flow, J. Eur. Ceram. Soc. 24 (10) (2004) 3209–3218, https://doi.org/10.1016/j.jeurceramsoc.2003.11.014.
[75] V. Salvini, M.D.M. Innocentini, V.C. Pandolfelli, Optimizing permeability, mechanical strength or ceramic foams, Am. Ceram. Soc. Bull. 79 (5) (2000) 49–54.
[76] P. Sepulveda, F.S. Ortega, M.D.M. Innocentini, V.C. Pandolfelli, Properties of highly porous hydroxyapatite obtained by the gelcasting of foams, J. Am. Ceram. Soc. 83 (12) (2000) 3021–3024, https://doi.org/10.1111/j.1151-2916.2000.tb01677.x.
[77] M.D.M. Innocentini, J. Yamamoto, R.G. Ribeiro, et al., Effect of particle size distribution on the drying behavior of refractory castables, Cerâmica 47 (2001) 304.
[78] M.D.M. Innocentini, A.R. Studart, R.G. Pileggi, How PSD affects permeability of castables, Am. Ceram. Soc. Bull. 80 (5) (2001) 31–36.
[79] M.D.M. Innocentini, R. Salomao, C. Ribeiro, et al., Permeability of fiber-containing refractory castables, Am. Ceram. Soc. Bull. 81 (7) (2002) 34.
[80] M.D.M. Innocentini, A.R.F. Pardo, V.C. Pandolfelli, B.A. Menegazzo, L.R. M. Bittencourt, R.P. Rettore, Permeability of high-alumina refractory castables based on various hydraulic binders, J. Am. Ceram. Soc. 85 (6) (2002) 1517–1521, https://doi.org/10.1111/j.1151-2916.2002.tb00306.x.
[81] F.S. Ortega, M.D.M. Innocentini, F.A.O. Valenzuela, V.C. Pandolfelli, Effect of aeration technique on the macrostructure and permeability of gelcast ceramic foams, Cerâmica 48 (306) (2002) 79–85.
[82] A.R. Studart, F.S. Ortega, M.D.M. Innocentini, V.C. Pandolfelli, Gelcasting high-alumina refractory castables, Am. Ceram. Soc. Bull. 81 (2) (2002) 41–47.

[83] I.F. Macdonald, M.S. El-Sayed, K. Mow, F.A.L. Dullien, Flow through porous media—the ergun equation revisited, Ind. Eng. Chem. Fundam. 18 (3) (1979) 199–208, https://doi.org/10.1021/i160071a001.
[84] N. Ahmed, D. Sunada, Nonlinear flow in porous media, J. Hydraul. Div. 95 (6) (1969) 1847–1858.
[85] Darcy H. Les fontaines publiques de la ville de dijon (the public fountains of the city of Dijon). 1856.
[86] C. Huber, Y. Su, A pore-scale investigation of the dynamic response of saturated porous media to transient stresses, Geofluids 15 (1–2) (2015) 11–23, https://doi.org/10.1111/GFL.12087.
[87] R.A. Wooding, Steady state free thermal convection of liquid in a saturated permeable medium, 2006/03/28, J. Fluid Mech. 2 (3) (1957) 273–285, https://doi.org/10.1017/S0022112057000129.
[88] D.M. Hyman, M.I. Bursik, E.B. Pitman, Pressure-driven gas flow in viscously deformable porous media: application to lava domes. 2019/04/18, J. Fluid Mech. 869 (2019) 85–109, https://doi.org/10.1017/jfm.2019.211.
[89] M. Eberstein, S. Reinsch, R. Müller, J. Deubener, W.A. Schiller, Sintering of glass matrix composites with small rigid inclusions, J. Eur. Ceram. Soc. 29 (12) (2009) 2469–2479.
[90] M.J. Pascual, A. Durán, M.O. Prado, et al., Model for sintering devitrifying glass particles with embedded rigid fibers, J. Am. Ceram. Soc. 88 (6) (2005) 1427–1434, https://doi.org/10.1111/j.1551-2916.2005.00322.x.
[91] P.N. Sen, C. Straley, W.E. Kenyon, M.S. Whittingham, Surface-to-volume ratio, charge density, nuclear magnetic relaxation, and permeability in clay-bearing sandstones, Geophysics 55 (1) (1990) 61–69, https://doi.org/10.1190/1.1442772.
[92] M. Firouzi, K. Alnoaimi, A. Kovscek, J. Wilcox, Klinkenberg effect on predicting and measuring helium permeability in gas shales, Int. J. Coal Geol. 123 (2014) 62–68, https://doi.org/10.1016/j.coal.2013.09.006.
[93] J. Vasseur, F.B. Wadsworth, Y. Lavallée, A.F. Bell, I.G. Main, D.B. Dingwell, Heterogeneity: the key to failure forecasting, Sci. Rep. 5 (1) (2015) 13259, https://doi.org/10.1038/srep13259.